CARRIER MANIPULATION IN GRAPHENE/FERROELECTRIC HYBRID STRUCTURES

BY

CHRISTOPH BAEUMER

THESIS

Submitted in partial fulfillment of the requirements
for the degree of Master of Science in Materials Science and Engineering
in the Graduate College of the
University of Illinois at Urbana-Champaign, 2013

Urbana, Illinois

Advisers:

Associate Professor Moonsub Shim
Assistant Professor Lane W. Martin

Abstract

The combination of two novel classes of functional materials with exciting prospects for future nanoelectronic applications, i.e. carbon nanoelectronics and complex oxide thin film electronics, is expected to lead to a range of new phenomena being accessible for observation, scientific characterization and understanding, as well as for utilization in future electronic devices. This thesis reports significant advancement in the integration of two prominent representatives of these material classes - graphene and ferroelectric oxides.

First, the major road blocks complicating previous attempts to integrate graphene with ferroelectric oxides are identified. The hybrid devices fabricated so far suffered from extrinsic hysteresis effects from adsorbed molecules screening any coupling between the graphene charge carriers and the ferroelectric polarization. The experimental methods utilized to overcome these challenges are introduced for device fabrication and characterization.

The resulting graphene/$PbZr_{0.2}Ti_{0.8}O_3$ hybrid structures presented here exhibit bidirectional interdependency between the graphene doping level and the ferroelectric polarization. Using graphene-based electrodes, the polarization of the $PbZr_{0.2}Ti_{0.8}O_3$ can be switched reliably and fast with low voltages, which in turn can change the doping level in graphene channels. One of the most striking consequences of ferroelectric polarization switching dominating electron transport in graphene is the complete reversal of the hysteresis direction in transistor devices. This reversible and permanent switching behavior can now be used in non-volatile ferroelectric graphene transistors.

To overcome the low on/off ratio of these devices, a utilization of complex domain structures underlying a graphene transistor channel is explored for novel carrier manipulation. Through the detailed characterization with Raman spectroscopy and scanning photocurrent measurements, the creation of potential steps in graphene at domain walls of the underlying ferroelectric is demonstrated. Carrier density modulations of approximately 5×10^{12} cm^{-2} now provide a platform that offers graphene devices exhibiting potential steps which can be tuned from p^+-p to p-n to n-n^+ junctions through the application of a single gate for the entire channel area. This is particularly useful for the implementation and utilization of the exciting two-dimensional phenomena in graphene.

To Laura, for your unconditional love and support that does not know borders but crosses continents.

To my parents, for awakening my scientific curiosity and helping me find my way through education while remembering what really is important in life.

Acknowledgments

I would like to give special thanks to my advisors, Professors Moonsub Shim and Lane W. Martin, who have been an inspiration in many ways. You deepened my love and pursuit of the understanding of natural phenomena, the true basis of Materials Science. Your continuous support and advice on science, scientific procedures and personal matters will always remain an important part of my life and professional development.

I would also like to thank my lab mates for a perfect environment for working and learning. Especially, I would like to thank Steven Rogers for many great discussions and ideas, in particular while enjoying tea or coffee during a break. Thank you to Johnathon Tsai, Karthik Jambunathan and Anoop Damodaran for teaching me so much about science, graduate school, and life.

Many thanks to the staff scientists at MRL for their continuous efforts to enable cutting-edge research.

Table of Contents

LIST OF ABBREVIATIONS

AFM	Atomic force microscopy
CMOS	Complementary metal oxide semiconductor
FET	Field Effect Transistor
PEI	Poly(ethylenimine)
PEO	Poly(ethylene oxide)
PFM	Piezoresponse force microscopy
PMMA	Poly(methyl methacrylate)
PUND	Positive Up Negative Down

Chapter 1

Introduction

Graphene, a two-dimensional sheet of carbon atoms with unparalleled electronic properties such as extremely high carrier mobilities, has become an intriguing platform for leveraging exotic low-dimensional phenomena for advanced functionality since its discovery in 2004 [1–7]. Recent advances in large-area chemical vapor deposition growth and transfer to arbitrary substrates now allow for fabrication of wafer-scale graphene device arrays [8, 9]. Experimental observation, and ultimately practical implementation, of unique phenomena associated with massless Dirac fermions in graphene, however, is difficult and often requires a suite of sophisticated instrumentation [4–7]. Furthermore, even the most mundane exploitation of graphene as a high-mobility channel in conventional field-effect transistors (FETs) is limited due to its zero-gap nature [3].

Therefore, a more sophisticated device structure is necessary to utilize the promising electronic properties in graphene devices. One possible route towards the creation of a transport gap in graphene is the utilization of the highly angle-dependent quantum tunneling across p-n-junctions in graphene, which is caused by the chiral nature of the massless Dirac fermions [6, 10]. Interfacing graphene, the prototype of the still young but extremely fast growing field of carbon electronics, with the more traditional field of electronic complex oxide thin films such as ferroelectrics may therefore open new means of carrier manipulation in graphene to enable the exploitation of its unparalleled two-dimensional electronic properties for such next generation devices.

Ferroelectric oxide thin films are suitable for high-speed nonvolatile memories, high-density capacitors, and advanced low-power logic elements due to their high susceptibility and large, electric-field controllable remanent polarization [11–14]. Recent developments in the synthesis of complex oxide thin films allow for nanometer-scale artificial structures compatible with low-power semiconductor technology [15–18]. The accessibility of nano-patterned domain structures in ferroelectric thin films may open ways toward nano-scale carrier manipulation in graphene devices, if it can be shown that the doping level of graphene channels on such oxide films can be controlled through the ferroelectric polarization.

Previous studies of graphene incorporated into FETs with ferroelectric gates have revealed a strong interaction between the gate dielectric and graphene leading to potentially useful attributes such as stable hysteresis curves or nonvolatile changes in the carrier density [19–26]; however, the observed characteristics of graphene on ferroelectric oxides have been attributed to extrinsic charging effects rather than a direct coupling of the ferroelectric polarization to charge carriers in graphene [19–22], similar to hysteresis effects of graphene and carbon nanotube devices on non-ferroelectric substrates. Extrinsic hysteresis effects, mostly associated with slow motion of adsorbed molecules, opposing the ferroelectric polarization and their delayed response compared to ferroelectric switching are undesirable aspects that complicate our understanding of graphene/ferroelectric interactions and therefore currently limit the applicability of this system.

Therefore, it is the goal of this thesis to unambiguously identify and overcome major road blocks in the combination of carbon and oxide electronics and to demonstrate that interfacing graphene with ferroelectric oxides can indeed lead to next generation switches through complex carrier manipulation. Based on previous results on graphene and $PbZr_{0.2}Ti_{0.8}O_3$, certain open questions need to be addressed to show

that the integration of graphene and complex oxide thin films can actually lead to the desired leap in nanoelectronic research:

1. Ferroelectric switching in thin films with graphene based electrodes must be demonstrated to prove that the ferroelectric film does not lose its defining characteristic due to poor contact properties.

2. The extrinsic hysteresis effects observed previously need to be overcome so that the ferroelectric polarization can directly control the carrier density in the graphene film.

3. Local control of the graphene doping level through to the underlying potential landscape exerted by a polydomain ferroelectric has to be demonstrated to prove that these hybrid structures can be used for the spatial modulation of the carrier density and therefore for next generation graphene electronics.

The current state of the scientific understanding of graphene/ferroelectric hybrid structures will be presented in Chapter 2. The open questions 1 and 2 will be addressed by the development of novel fabrication methods of hybrid structures of graphene and $PbZr_{0.2}Ti_{0.8}O_3$ [Chapter 3] and their detailed characterization in Chapter 4. Stable and reversible ferroelectric operation in both capacitor and FET geometries is shown, revealing how contributions from surface/interface charging and adsorbed molecules can be separated from the intrinsic interaction and how they can be sufficiently reduced to allow observation of direct effects of ferroelectric polarization on single-layer graphene. A complete reversal of the direction of the hysteresis in the transfer characteristics allows for reversible and permanent switching of the resistance state of the graphene channel through ferroelectric switching.

A proof of concept for spatial carrier modulation is provided in Chapter 5 with periodically doped graphene on commercially available periodically poled $LiNbO_3$ single

crystals and implemented to arbitrarily writable domain structures in $PbZr_{0.2}Ti_{0.8}O_3$ thin films. The local control of carrier density through the polarization direction of the underlying substrate now provides the basis for the development of graphene transistors exhibiting spatial carrier density modulation, which may open the way towards a transport gap and other device designs utilizing spatial carrier modulation, such as the utilization of collective excitations, which exhibit low energy loss compared to dissipative charge transport.

This thesis is part of the on-going interdisciplinary "Research on Nanoelectronics for 2020 and Beyond" supported by the National Science Foundation and the Semiconductor Research Alliance in the project "Meta-Capacitance and Spatially Periodic Electronic Excitation Devices". The goal of this project is to create a new generation of low-power, high on-off current ratio, fast response switches by bridging different nanoelectronic disciplines.

Chapter 2

State of the Art in Graphene and Complex Oxide Electronics

2.1 Graphene: Properties and Devices

Graphene, a two dimensional monolayer of carbon atoms arranged in a hexagonal honeycomb lattice, exhibits a variety of desirable properties due to its unique structure. The sp^2 hybridazation also found in graphite leads to a trigonal planar lattice with σ bonds between two carbon atoms and a delocalized, half filled π band [3]. The existence of this two dimensional electron gas in the absence of interaction with additional graphite layers leads to the exceptional electron dispersion in graphene, which has been described analytically for the first time by P.R. Wallace in 1947 [27]. As can be seen in figure 2.1, the electron (hole) energy close to the corners of the hexagonal Brillouin zone, the so-called Dirac points, increases (decreases) linearly with k. Therefore, low energy excitations in graphene are so-called massless, chiral Dirac fermions [3], which behave differently from ordinary electrons. Following the physics of quantum electrodynamics, they exhibit unique behavior in magnetic fields, experimentally shown in the anomalous integer and fractional quantum hall effects [4,5], and external electric potentials, penetrating classically forbidden regions with angle dependent transmission probabilities up to 100 % [6].

The absence of a rest mass of charge carriers in graphene is the reason for the observed extremely high electron and hole mobilities even for high doping levels, leading to ballistic or lossless transport on the micrometer scale [2]. This has led to major research interest in graphene, especially after wafer-scale device arrays have

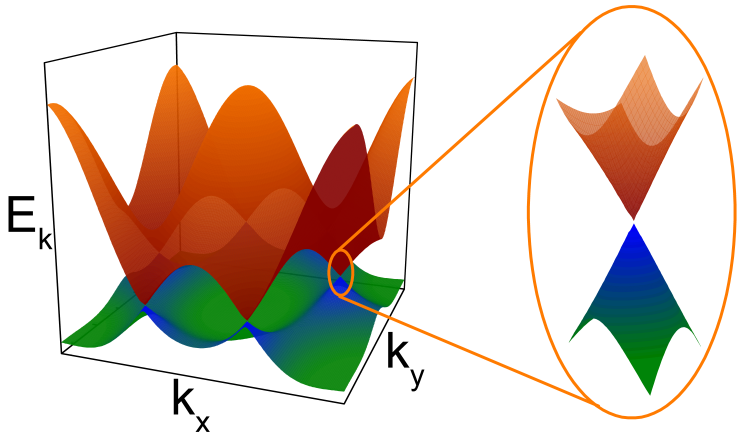

Figure 2.1: Band structure of graphene according to the tight-binding approach in ref [3]. Left: Energy spectrum in the vicinity of the first Brillouin zone. Right: Zoom in the electronic dispersion around one of the Dirac points.

been made possible through the development of chemical vapor grown graphene and its transfer to arbitrary substrates, compare section 3.1.2. The transfer characteristics (drain current I_D versus gate voltage V_G curve) of the most-widely studied graphene device, a FET with a graphene channel fabricated on a Si/SiO_2 wafer, utilizing the Si as a back-gate electrode and the SiO_2 as a gate dielectric, is depicted in figure 2.2. The ambipolar behavior of graphene can be clearly seen in the "v-shape" of the transfer curve. The minimum in the conduction corresponds to the fermi level being aligned with the Dirac point. A positive offset of the gate voltage necessary to reach this indicates a p-doped graphene channel, which is the typical result in ambient air. The

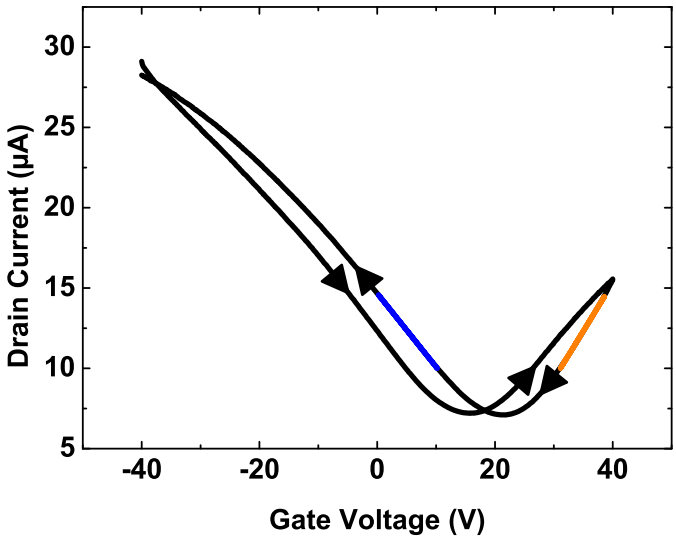

Figure 2.2: Transfer characteristic for a characteristic back-gated graphene FET with 300 nm SiO_2 gate dielectric. Linear fits to the transconductance in the hole and electron regime (blue line and orange line, respectively) reveal a electron (hole) mobility of $1248(955)\,\mathrm{cm^2V^{-1}s^{-1}}$. Black arrows indicate the sweep direction. A significant hysteresis manifests itself in the Dirac point shift of 6.2 V towards more positive gate voltages, corresponding to a carrier density change of $\sim$5x10^{11} $\mathrm{cm^{-2}}$.

linear regime in the transfer curve can be utilized to calculate the mobility μ of a particular device from the transconductance g_m:

$$g_m = \frac{\Delta I_D}{\Delta V_G} \tag{2.1}$$

$$\mu = \frac{g_m L}{V_D W C_{Ox}} \tag{2.2}$$

with the drain current I_D, the gate voltage V_G, the channel length and width L and W, the drain voltage V_D and the gate oxide areal capacitance C_{Ox}. See ref. [28] for a detailed derivation. Linear fits to the transconductance in the hole and electron regime (blue line and orange line, respectively) reveal an electron (hole) mobility of 1248 (955) $\mathrm{cm^2V^{-1}s^{-1}}$ for the device shown in figure 2.2.

The exploitation of the unparalleled mobilities achievable in graphene as a high-mobility channel in the traditional FET geometry, however, is limited due to several

reasons. Firstly, because of its zero gap nature, graphene exhibits a finite conductance minimum with a theoretical value of $\sigma_{min} = \frac{4e^2}{h\pi}$, severely limiting the maximum on/off ratio [2]. Experiments have not yet been able to even achieve this value, which can be attributed to the fact that due to local potential variations a graphene channel can never be entirely intrinsic but rather consists of so-called electron and hole puddles. This mechanism, which has been connected to local charge density variations of the substrate through measurements of the spatial distribution of the Dirac point, explains the broad minimum in the conductance [figure 2.2] because different areas of the channel reach their conductance minimum for slightly different gate voltages.

Secondly, the mobility in graphene is commonly reduced significantly from theoretical values through defects, which are common for CVD grown graphene [29], interaction with the substrate [30] and scattering due to adsorbents from the ambient environment or polymer residues from transfer and lithography processes [31]. The highest mobilities so far have therefore been reported for suspended graphene [32] or graphene on hexagonal boron nitride, which reduces substrate induced scattering because of its atomic flatness [33].

Moreover, devices fabricated on commonly used gate oxides exhibit a non-negligible hysteresis between forward and reverse gate voltage sweeps [figure 2.2]. Several mechanisms have been shown to cause such a hysteresis in the extensively studied graphene and carbon nanotube on SiO_2 devices, such as the relatively slow interactions with surrounding molecules like H_2O and O_2 [34–37], charge injection into interfacial trap states [38–40], and/or charge redistribution within the substrate caused by mobile and trapped charges [41]. In ambient air, these extrinsic factors result in a hysteresis between two p-type states for electric field or gate voltage cycles. Upon application of a positive gate voltage, the system exhibits enhanced p-doping, corresponding to a positive shift of the Dirac point in the transfer characteristics going from the forward

to the reverse sweep. These hysteresis effects severely complicate our understanding and the applicability of graphene-based devices.

A more complex behavior is expected for more advanced graphene based devices, for example in channels exhibiting one or multiple p-n-junctions. As mentioned before, because the electrons in graphene behave according to quantum electrodynamics, they can be transmitted through classically forbidden regions. In fact, the charge carriers can be transmitted through a p-n-junction with 100 % probability if they are traveling normal to the junction [6]. At different angles ϕ the transmission probability of an electron of energy E through a potential barrier of height V_0 and width D is given by

$$T(\phi) = \frac{\cos^2\theta\cos^2\phi}{\left[\cos(Dq_x)\cos\phi\cos\theta\right]^2 + \sin^2(Dq_x)\left(1 - ss'\sin\phi\sin\theta\right)^2} \tag{2.3}$$

with $\theta = \arctan\left(\frac{k_y}{q_x}\right)$, $q_x = \sqrt{\frac{(V_0-E)^2}{v_f^2} - k_y^2}$, $s = \mathrm{sgn}(E)$, $s' = \mathrm{sgn}(E - V_0)$ and the fermi velocity $v_f \approx 1 \times 10^6$ m s^{-1} [3]. The existence of this so-called chiral tunneling has been proven experimentally for normal and slanted p-n-junctions in single layer graphene [42] [10]. This angle dependent tunneling now allows for the ability to focus electrons similar to Snell's law in classical optics [43] and potentially the opening of a transport gap in graphene transistors with a suitable set of local gates, which has been suggested by Katsnelson *et al.* in 2006 [6]. This would open the way towards device implementation of graphene for next generation nano electronics. But this implementation also requires ballistic transport throughout multiple junctions, which might be one of the reasons why graphene devices with a transport gap have not yet been experimentally realized. Additionally, charge density inhomogeneities caused by local surface potential fluctuations of the underlying substrate and adsorbed molecules further complicate experimental implementation of sharp p-n-junctions.

2.2 Ferroelectric Thin Films

Ferroelectric materials are a sub-class of dielectric materials which exhibit a spontaneous electric polarization that can be reoriented between crystallographic directions through the application of external electric fields [44]. Although the phenomenon has been known since the 1920s, major interest into ferroelectricity was stimulated through the discovery of ferroelectric perovskite structures such as $BaTiO_3$ or $PbZr_{0.2}Ti_{0.8}O_3$ in 1943 due to the availability and robustness of these oxides [12]. The development of thin-film ferroelectrics, especially their integration into semiconductor technology, led to another major leap in the application of ferroelectrics, leading to high-speed nonvolatile memories, high-density capacitors, and advanced low-power logic elements [11–14].

At high temperatures, typical ferroelectric oxides exist in a cubic perovskite structure [figure 2.3]. At the so-called Curie temperature T_c, a structural distortion gives rise to the creation of a polar crystallographic axis. For the model ferroelectric $PbZr_{0.2}Ti_{0.8}O_3$, the crystal structure below T_c is tetragonally distorted, with the spontaneous polarization along the tetragonal axis [figure 2.3] [44].

The phase transition between these two states can be understood in terms of the condensation of the soft phonon mode in ionic crystals [44]. Due to the existence of internal electric fields, optical phonon modes are split into different energies. The longitudinal phonon mode frequency ω_{LO}^2 is hardened because the polarization field and the mechanical restoring force for each ion enhance each other, while they have opposite effects on the low-frequency transverse optical mode ω_{TO} according to

$$\omega_{TO}^2 = \omega_0^2 - \frac{1}{3}\omega_p^2 \cdot \frac{\chi_\infty + 3}{3} \tag{2.4}$$

with the resonance frequency of the ions ω_0, their plasma frequency ω_p and the high-frequency limit of the electric susceptibility χ_∞. At the phase transition temperature,

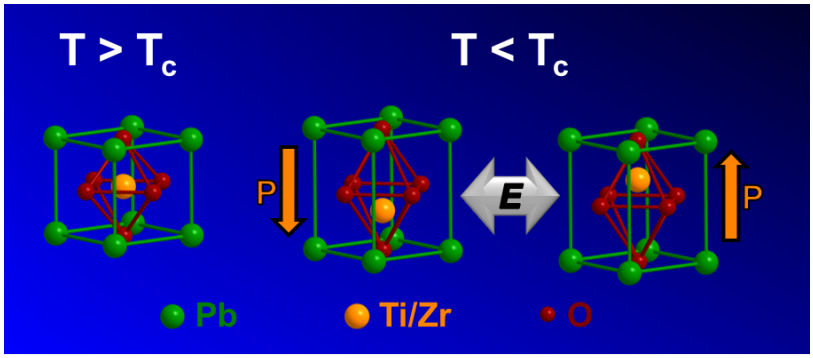

Figure 2.3: Crystal structure of $PbZr_{0.2}Ti_{0.8}O_3$ as a model ferroelectric perovskite. Above the Curie temperature T_c, the cubic phase is stable, leading to a paraelectric phase due to the existence of an inversion center at the center of the unit cell. Below T_c, a tetragonal distortions leads to the creation of a spontaneous polarization due to the separation of Ti/Zr and O sublattices. Through the application of an electric field the polarization direction can be reversed along the polar axis.

the opposing effects cancel each other out, leading to the condensation of this mode at the Brillouin zone center, i.e. the frequency goes to zero, while the wavelength becomes infinite. Therefore, the anion and cation sublattices are permanently displaced with respect to each other, giving rise to a spontaneous polarization.

In the absence of external fields or confining boundary conditions, all $\langle 100 \rangle$ directions are degenerate in $PbZr_{0.2}Ti_{0.8}O_3$; the octahedrally coordinated center Ti^{4+} ion can be displaced towards each of its six nearest neighbors. According to the Poisson equation, a so-called depolarization field would be observed because of the divergence of the polarization at the sample surfaces if the entire sample were polarized into the same direction [45]:

$$\nabla D = \rho \qquad \Rightarrow \qquad \nabla E = \frac{\rho - \nabla P_S}{\epsilon_0 \epsilon_r} \tag{2.5}$$

with the electric displacement D, the charge density ρ, electric field E, the spontaneous polarization P_S and the permittivity $\epsilon_0 \epsilon_r$ [45]. Therefore, all six possible orientation states coexist in bulk samples, minimizing the depolarization field. Regions of uniform polarization are called ferroelectric domains and are separated by

domain walls of 1 to 10 lattice parameters thickness. Due to the energy cost associated with the formation of domain walls, which can be regarded as a type of interface, and elastic distortions between different orientations, the formation of arbitrarily small domains is unstable. Instead, ferroelectrics generally exist in the domain configuration that allows for a minimization of the total energy [44].

For thin films, the stable domain configuration of a ferroelectric substrate can be tuned through a variety of external parameters, such as the composition, thickness, electrical boundary condition and the epitaxial strain. For $PbZr_{0.2}Ti_{0.8}O_3$ thin films grown on (001)-oriented substrates introducing compressive strain, the polarization is mostly oriented along the surface normal (c-domains) with a small fraction of domains with in-plane orientation (a-domains) [46].

When an electric field is applied to a ferroelectric, the energetic degeneracy of the possible polarization directions is broken, making the alignment of the polarization along the external field more favorable. Therefore, the polarization can be switched between at least two different directions. In $PbZr_{0.2}Ti_{0.8}O_3$ thin films, the c-domains change their polarization direction if a field is applied out-of-plane of the film. The conversion from one polarization state to the other takes place through a process of domain nucleation and growth through domain wall motion, which is described in detail in ref. [47]. The magnitude of the applied electric field generally governs the nucleation and growth times and therefore determines how long a specific field has to be applied to completely switch the polarization. The switching of the spontaneous polarization also leads to the characteristic hysteresis loop in the $P-E$ curve observed for ferroelectrics [figure 2.4]. For small applied fields, only the dielectric polarization changes, leading to small, linear change in the polarization with applied field. At the coercive field E_C, the spontaneous polarization reverses its sign, leading to a dramatic change in the overall polarization. Once the electric field is reduced to zero, only the

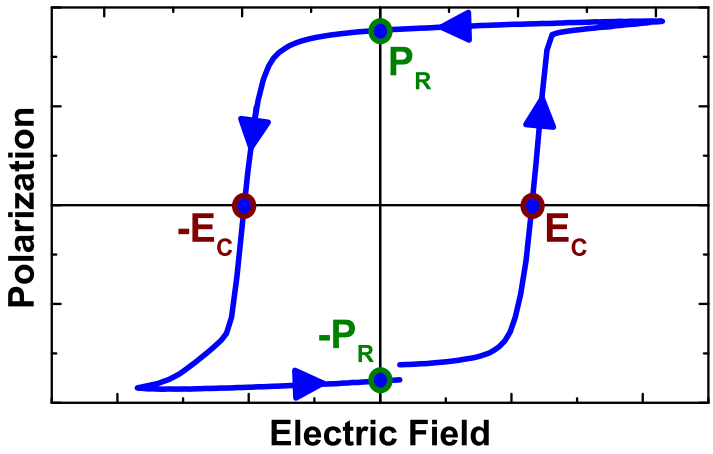

Figure 2.4: $P - E$ curve for a typical ferroelectric thin film with the coercive field E_C and the remanent polarization P_R.

spontaneous polarization remains. Therefore, it is commonly referred to as remanent polarization.

Because of the finite size of the domains, a non-zero depolarization field exists in most ferroelectric materials, which reduces the measurable ferroelectric polarization. The only possible way for the depolarization field to vanish is the existence of complete compensation of the surface charge density associated with the polarization. This can be achieved through free charges of the surrounding medium. In the case of metal contacts, the high charge density in the surrounding medium typically leads to a nearly complete compensation, while ferroelectric samples in air or contacted by media with a smaller carrier density severely suffer from a reduced remanent polarization due to large depolarization fields, as has been observed for semiconducting contacts [48].

2.3 Graphene/Ferroelectric hybrid Structures

In devices combining ferroelectric thin films as a gate dielectric with a graphene transistor channel, the graphene is expected to compensate the surface charge associated with the polarization. A non-volatile hysteritic behavior is expected in the graphene resistivity because of the hysteresis in the ferroelectric polarization, if the gate voltage exceeds the coercive field. The hysteresis direction in the case of direct coupling of the ferroelectric polarization and charge carriers in graphene is expected to be opposite from the extrinsic hysteresis characteristic commonly observed on substrates such as SiO_2 (compare section 2.1).

Poling the ferroelectric in an "up" state (with the polarization pointing toward the graphene) with a positive gate voltage should stabilize electrons in the graphene (making it n-type or at least less p-type) while poling the ferroelectric in the "down" state (with the polarization pointing away from the graphene) should stabilize holes (making the graphene more p-type). In other words, the electric field from the up-polarized $PbZr_{0.2}Ti_{0.8}O_3$ should create a positive offset in V_G leading to the Dirac point shifting to a more negative, rather than a more positive value. Given that the ferroelectric polarization of ferroelectric thin films such as $PbZr_{0.2}Ti_{0.8}O_3$ possess a remanent polarization corresponding to an enormous areal charge density of 5×10^{14} C·cm^{-2}, a very large doping effect in the graphene would be expected for the case of a perfect interface between both materials.

The first attempts to integrate graphene with ferroelectric materials began nearly simultaneously for oxide ferroelectrics - namely with the work by Hong *et al.* with graphene on $PbZr_{0.2}Ti_{0.8}O_3$ [19, 20] - and polymer ferroelectrics in the form of poly(vinylidene fluoride trifluoroethylene) by Zheng *et al.* [19, 23] in 2009. Organic ferroelectric materials offer the advantage of facile fabrication at low temperatures even on top of pre-fabricated graphene devices. Consequently, progress in the field of

organic ferroelectrics combined with graphene has been very fast, leading to transistor devices exhibiting non-volatile resistance hysteresis behavior [23, 26] and an effective mechanism has been proposed to control the doping level [25]. Devices on flexible and transparent substrates or with free-standing sandwich structures can now be used for various transparent electronics applications [24, 49].

Nevertheless, Zheng *et al.* also pointed out that for highest performance "inorganic ferroelectric (such as lead zirconate titanate)" should be used due to better endurance, lower coercive fields and faster writing speed compared to organic ferroelectrics. Furthermore, only the nanopatterning capabilities now available in thin film ferroelectric oxides [15–17] open the way towards carrier manipulation in graphene transistors going beyond simple, non-volatile memory application.

The work with these oxide thin films, however, has not led to as clear an understanding of the observed mechanisms to this point. Hong *et al.* first observed that few-layer-graphite, a stack of multiple graphene layers, exhibits high mobility on $PbZr_{0.2}Ti_{0.8}O_3$ thin films, which they attribute to a reduced scattering from adsorbates on the $PbZr_{0.2}Ti_{0.8}O_3$ due to ordering in the electric field of the ferroelectric [19]. The adsorbates present at the interface between graphene and $PbZr_{0.2}Ti_{0.8}O_3$ - which is a distinctive difference from the case of organic ferroelectrics fabricated directly on the graphene - makes the device performance rather complicated. Both few-layer and single-layer graphene devices suffer from a pronounced hysteresis caused by extrinsic charging because of these adsorbed molecules, which has made a direct control of the doping level of graphene through the ferroelectric polarization impossible up to now [20, 21].

The extensive previous research on graphene and ferroelectric thin films independently has shown that a combination of these material classes would provide a very suitable platform to leverage exotic nanoelectronic carrier properties. But

extrinsic hysteresis effects opposing the ferroelectric polarization, which have so far limited the understanding and applicability of graphene/ferroelectric oxide heterostructures, need to be overcome to realize the promising phenomena expected from the combination of carbon and oxide electronics.

Chapter 3

Experimental Methods

In this chapter, the experimental details for sample fabrication and characterization, which have been used to overcome the challenges in the implementation and application of graphene/ferroelectric hybrid structures (section 2.3), are summarized. An optimized transfer process of chemical vapor deposition grown graphene to pulsed laser deposition grown ferroelectric films has been developed and utilized for the fabrication of capacitors and transistors. These are characterized structurally and electrically through x-ray diffraction, scanning probe microscopy, Raman spectroscopy and electrical transport measurements.

3.1 Sample Preparation

3.1.1 Pulsed Laser Deposition of Ferroelectric Thin Films

Pulsed laser deposition is a versatile physical vapor deposition technique enabling the deposition of thin films with high crystalline quality and desired stoichiometry. In this process, a target of the same stoichiometry as the desired thin film is evaporated by a laser in a vacuum chamber in the presence of process gases such as oxygen or ozone. The laser energy is adjustable using a apertures and attenuators in the optical path. The energy transfer on the order of $1\,\mathrm{J\,cm^{-2}}$ causes the target material to ablate and form a plasma. A directed plasma plume toward the substrate is formed, which contains a jet of material that is oriented normal to target and substrate. The ablation

takes place far away from thermodynamic equilibrium because of the high energy involved. Therefore it can be independent of the respective partial pressures of the constituents and is frequently regarded as nearly stoichiometric, although special care must be taken to achieve exact stoichiometry [50]. The kinetic energy of the plasma is determined by an interaction of the energy input by the laser pulses and inelastic collisions with gas molecules in the chamber, which is referred to as thermalization. Upon contact with the substrate, the plasma species are highly mobile on the pre-heated substrate, enabling epitaxial film growth through layer-by-layer or step flow growth mechanisms under carefully chosen conditions. The technique and growth mechanisms are described in detail in ref. [51].

For the hybrid structures examined in this thesis, 60 nm $SrRuO_3$ bottom electrodes and 140 nm $PbZr_{0.2}Ti_{0.8}O_3$ films were grown in a two-step *in situ* pulsed laser deposition process on $SrTiO_3$ (001) substrates employing a KrF excimer laser (wavelength $\lambda = 248\,\text{nm}$) at temperatures of 640 and 635 °C, laser repetition rates of 14 and 1 Hz, and laser fluences of 0.66 and 0.76 J cm^{-2} in oxygen atmospheres of 100 and 200 mTorr, respectively. After growth, the films were cooled to room temperature at an oxygen pressure of 760 Torr.

3.1.2 Chemical Vapor Deposition of Graphene

Chemical vapor deposition is an easily scalable, well established synthesis method yielding highly uniform films with low defect density and is compatible with the standard processes of the complementary metal oxide semiconductor (CMOS) technology, which makes it a highly suitable candidate for graphene synthesis, especially compared to mechanical exfoliation, which yields only small graphene flakes on the range of several micrometers [44, 52]. In standard thermal chemical vapor deposition processes, films are grown through the reaction of precursor gases with a substrate

material. The reaction is generally aided by the presence of catalysts and utilizes the thermal energy of both the heated substrate and the heated precursor molecules.

In single-layer graphene growth in particular, transition metal oxides with low carbon solubility such as Cu are utilized as a substrate. A gaseous carbon source like methane is thermally decomposed at the Cu surface in the presence of hydrogen, where the carbon atoms arrange in graphene nucleates. Throughout the process, a continuous graphene film grows on the Cu surface. Due to the low solubility of carbon in copper, the growth of a second layer of graphene is much less kinetically accessible, making the process self-limiting if the growth conditions are chosen correctly [8].

For the examination of graphene/ferroelectric hybrid structures, chemical vapor deposition grown single-layer graphene was chosen over mechanically exfoliated graphene due to easier device fabrication, repeatable interface characteristics, and larger accessible graphene pieces, covering up to 90 % of the ferroelectric surface. Single-layer graphene with low defect density was grown on ultra-pure Cu foils (Alfa Aesar 10950) similar to "recipe B" of ref. [9] in a quartz tube furnace. After annealing in 300 mtorr hydrogen atmosphere (flow rate $7\,\mathrm{cm^3{\cdot}min^{-1}}$) at 1000 °C for 30 minutes, a flow of $60\,\mathrm{cm^3{\cdot}min^{-1}}$ CH_4 was introduced in the quartz tube while the H_2 flow was maintained. After 20 minutes, the reaction tube was cooled rapidly to room temperature (approximately 100-150 °C·min^{-1}) *via* a cooling fan in the vicinity of the quartz tube while both gases remained flowing. The gas flow was turned off after the furnace had reached a temperature below 100 °C. Low defect density, continuity of the film and absence of multi-layer graphene are confirmed using Raman spectroscopy and atomic force microscopy (compare sections 3.2.3 and 3.2.1).

3.1.3 Graphene Transfer to Arbitrary Substrates

In order to fabricate graphene devices, the monolayer needs to be transferred onto the desired substrate or layered structure. Since the growth of single-layer graphene

on copper foils was first reported in 2009, the method of choice has been to spin-coat poly(methyl methacrylate) (PMMA) on the graphene before etching away the Cu foil [8]. The graphene/PMMA stack can then be transferred from the etchant solution to a clean water bath and subsequently deposited onto the substrate of choice. After the sample is dried, the PMMA is dissolved in acetone releasing the graphene on the new substate.

Because of the drawbacks of this method such as polymer residues on the graphene surface, which might alter its electrical properties [53], and the fact that previous research revealed the importance of the interface in graphene/ferroelectric hybrid structures (compare section 2.3), the common transfer method was modified to improve coupling between graphene and the ferroelectric thin film by minimizing metal-ion and organic residues at the interface. PMMA (A2 495K, Microchem Crop.) was spin-coated onto the Cu foil at 3000 rpm for 30 s after growth. Graphene on the back side of the Cu foil was removed using oxygen plasma treatment. The Cu/-graphene/PMMA stack was carefully placed onto 10 ml of etchant solution of 1 M aqueous ammonium persulfate in a specially designed beaker with an inlet and an outlet with stopcocks [figure 3.1]. When the Cu was etched away entirely, the fluid level in the beaker was slowly raised by pumping in 300 ml de-ionized water at a slow, steady rate from the bottom. The solution was allowed to flow out of the beaker as soon as the graphene/PMMA stack floated above the outlet. Once all of the etchant solution was replaced by de-ionized water, the graphene/PMMA stack was readied for transfer onto the desired substrate by thorough rinsing with de-ionized water in the same beaker without any intermediate lifting off from the water surface.

Meanwhile, the ferroelectric substrate, for example a $PbZr_{0.2}Ti_{0.8}O_3$ film, was cleaned by sonication in an acetone bath and oxygen plasma treatment. After the oxygen plasma treatment it was stored in acetone and kept in the bath until the graphene was ready for deposition. The ferroelectric was then rinsed with 2-propanol and im-

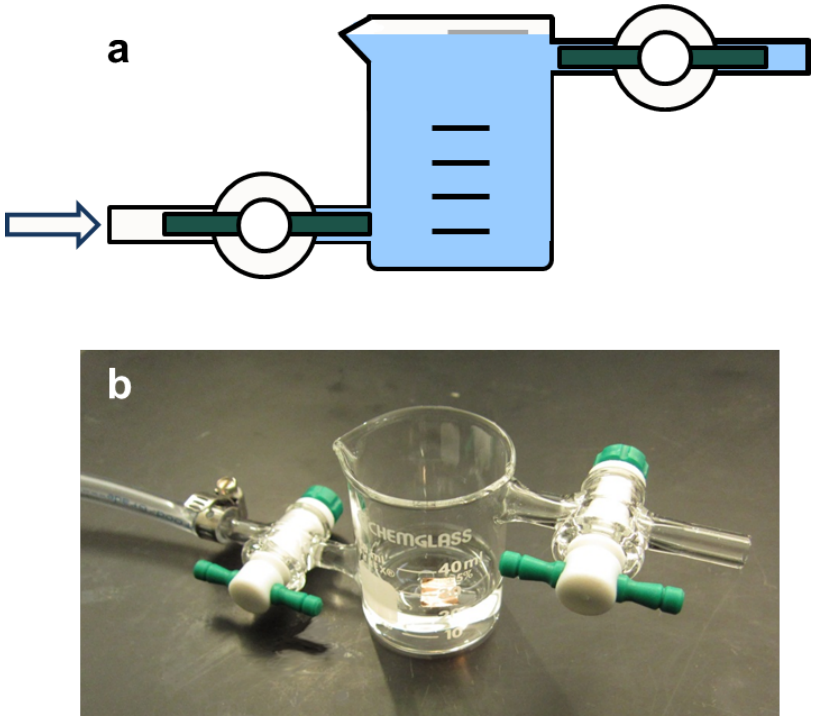

Figure 3.1: Modified graphene transfer method. a) Schematic of the one-touch transfer process. After the Cu foil is completely etched, de-ionized water is inserted into the beaker at a slow, steady rate from the bottom, flowing out of the beaker as soon as the graphene/PMMA stack floats above the outlet. b) Optical image of the specially designed beaker with an inlet and an outlet with stopcocks. The Cu/graphene/PMMA stack floats on the surface of the etchant solution.

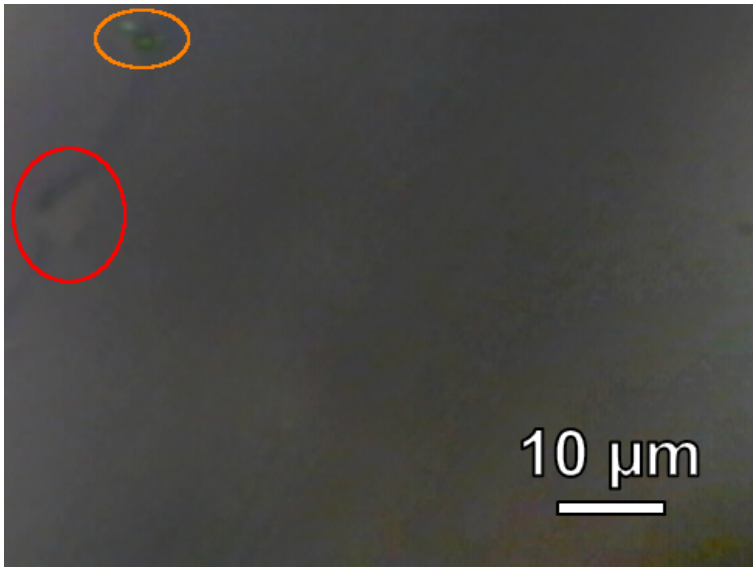

Figure 3.2: Optical image of a graphene film transferred to SiO_2. Due to differences in the light interference with the SiO_2 layer, the graphene appears darker than the bare SiO_2 surface, which can be seen in the transfer induced hole in the upper left corner (highlighted with a red ellipse). A transfer-induced residue particle is also clearly visible in the upper left corner (highlighted in orange). The diagonal, dark line between the hole and the residue corresponds to a grain boundary within the graphene film.

mersed into the DI water bath without allowing it to dry. The graphene/PMMA stack was transferred onto the substrate by raising the oxide from below. After carefully blow-drying the sample with dry nitrogen, it was allowed to dry overnight. The PMMA was then dissolved in a series of three acetone baths, a 30-min. bath in n-methyl pyrrolidinone and a 10-min. bath in 2-propanol at room temperature.

This transfer and cleaning procedure results in a more favorable interface as compared to traditional graphene transfer as discussed in section 4.2 and a comparably clean graphene surface as depicted in figure 3.2. Only small amounts of transfer-induced residue particles can be detected with an optical microscope. A more detailed characterization was performed using atomic force microscopy and is presented in section 3.2.1.

3.1.4 Device Fabrication

In a first step, circular capacitors were fabricated *via* standard photolithography and electron beam evaporation of Pd on a $PbZr_{0.2}Ti_{0.8}O_3$ film covered with graphene and on a separate $PbZr_{0.2}Ti_{0.8}O_3$ film grown simultaneously [figure 3.3]. Subsequent oxygen plasma treatment after dissolution of the photoresist was used to remove the excess graphene surrounding the capacitors. The choice of Pd as a top contact metal was motivated by its good adhesion properties to $PbZr_{0.2}Ti_{0.8}O_3$ and its beneficial work function offset with respect to the $PbZr_{0.2}Ti_{0.8}O_3$ film and the bottom electrode, leading to symmetric and low leakage current compared to contacts involving a common wetting layer such as Cr or Ti [compare Chapter 4] [54, 55]. The final device structure is shown in figure 3.4a.

In a second device structure, a series of photolithography and metallization steps was carried out to create the device structure shown in figure 3.4b. First, pairs of 100×100 μm^2 square pattern windows were opened through photolithography. The graphene exposed through these windows was removed using oxygen plasma. Afterwards, 100 nm SiO_2, 3 nm Ti and 20 nm Pd were deposited sequentially by electron beam evaporation to define the contact pads that were isolated from $PbZr_{0.2}Ti_{0.8}O_3$ [figure 3.3].

After lift-off, 50 nm thick Pd electrodes were patterned to connect graphene to these contact pads. In the last step, graphene was striped by oxygen plasma to define channels of 2.5 μm length and 5 μm width as well as to isolate devices.

In a last device geometry, 3 nm Ti/50 nm Pd electrodes were deposited onto graphene films transferred to various domain structures of $LiNbO_3$ single crystals using a shadow mask to prevent contamination from photoresist residues [figure 3.5]. Control devices were fabricated on the top surface of single crystals, which were all-down polarized and all up-polarized. Additionally, devices were fabricated on

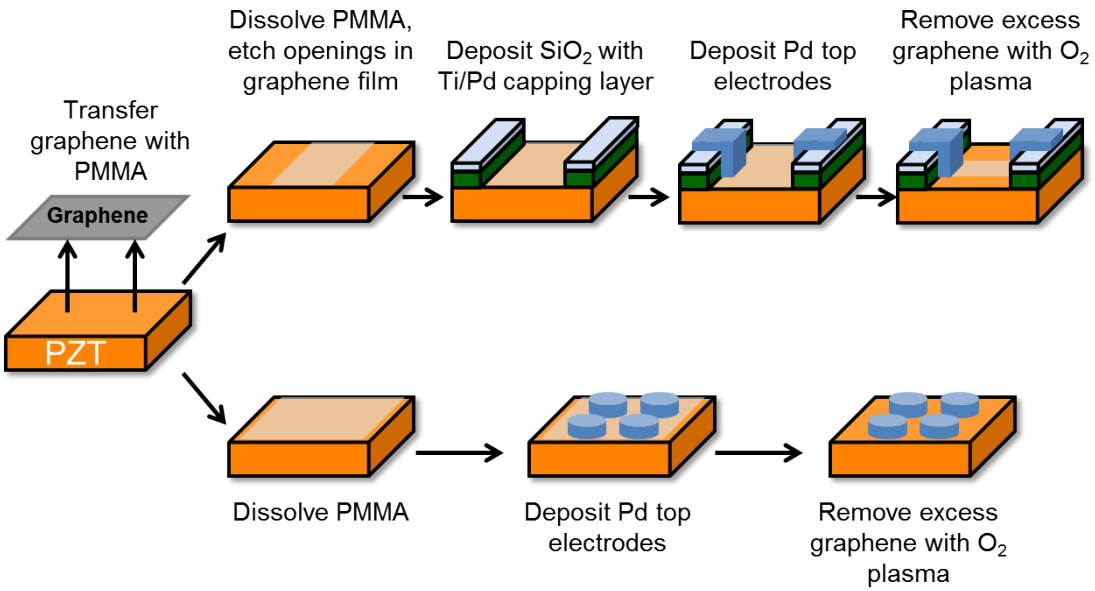

Figure 3.3: Fabrication of graphene transistors and capacitors. Graphene is transferred to $PbZr_{0.2}Ti_{0.8}O_3$ using the one-touch transfer described above. A series of photolithography, electron beam evaporation and oxygen plasma treatment leads to the desired device designs.

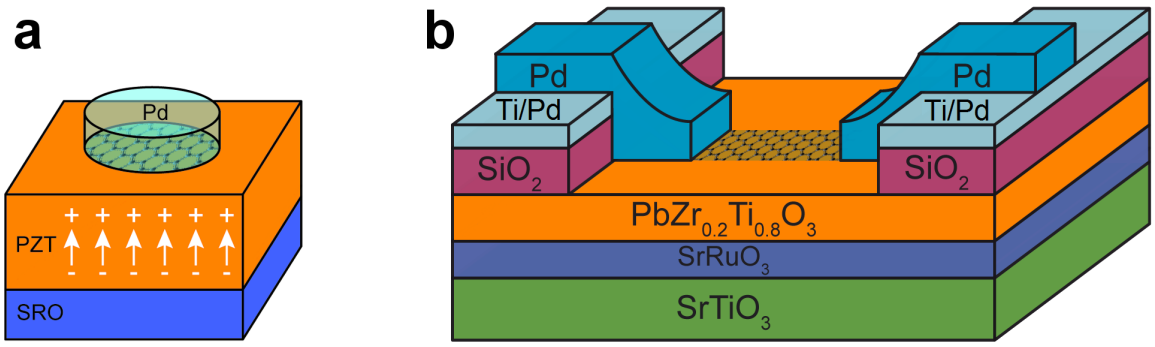

Figure 3.4: Graphene/$PbZr_{0.2}Ti_{0.8}O_3$ (PZT) hybrid devices. a) Capacitor structure contacted with a Pd top electrode deposited *via* electron beam evaporation. The $SrRuO_3$ (SRO) serves as the bottom in this parallel plate capacitor. b) Transistor structure with a graphene channel on a $PbZr_{0.2}Ti_{0.8}O_3$ thin film serving as the ferroelectric gate dielectric. The channel is contacted with Pd source and drain electrodes and a $SrRuO_3$ gate electrode. The device geometry includes an insulating SiO_2 layer to ensure low leakage current between the gate electrode and metal contact pads.

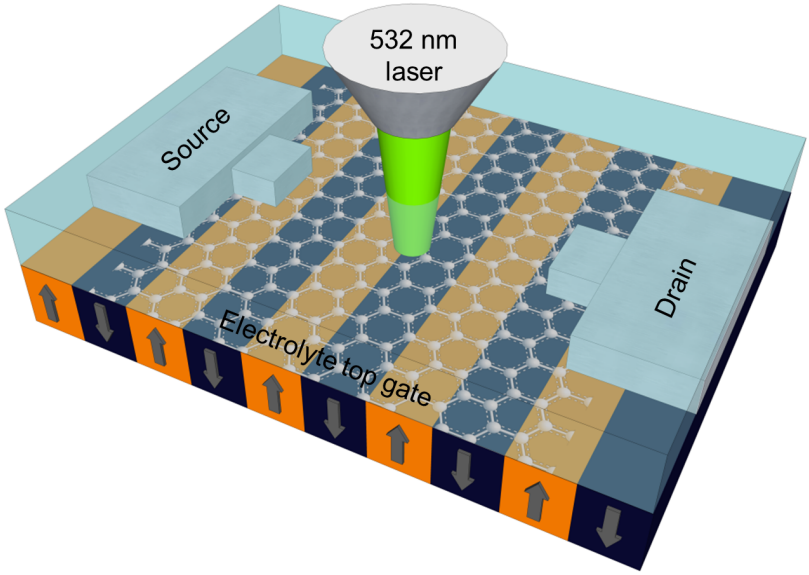

Figure 3.5: Top-gated graphene transistors on $LiNbO_3$. Graphene on different domain structures of $LiNbO_3$ was contacted with Ti/Pd source and drain electrodes and an electrolyte gate. The domain structure depicted here is periodically poled, pointing either towards or away from the graphene. The structures were characterized using Raman spectroscopy with 532 nm laser excitation (compare section 3.2.3).

commercially available periodically poled-up and -down $LiNbO_3$ (Asylum Research). The devices were characterized in air or with an electrolyte top gate. For gate-dependent measurements, polymer electrolytes were synthesized by the dissolution of $LiClO_4 \cdot 3H_2O$ in poly(ethylene oxide) (PEO, Sigma Aldrich, average molecular weight $M_v = 100,000$) in acetonitrile with $2.4 : 1 : 10$ polymer to salt to solvent weight ratios similar to references [56] and [57]. The electrolyte solution was spin-coated onto the graphene devices at 3000 rpm for 30 seconds.

3.2 Characterization

3.2.1 Scanning Probe Microscopy

Scanning probe microscopy was used in two separate ways for sample characterization. Firstly, topography images were obtained using atomic force microscopy (AFM) tapping mode scans. In this technique, a fine tip situated on a bar-like spring is scanned across the sample surface while detecting changes in the frequency and amplitude of its oscillation through the interaction forces between the tip and the specimen. A detailed description of atomic force microscopy can be found in ref [58]. A topography image of graphene transferred to the commonly used SiO_2 reveals negligible amounts of organic residues from the transfer process as well as clearly defined grain boundaries [figure 3.6a], confirming the cleanliness of the transfer process. A somewhat larger amount of residues is detected on graphene films transferred to $PbZr_{0.2}Ti_{0.8}O_3$ thin films [figure 3.6b]. This might be caused by enhanced electrostatic interaction between graphene and PMMA due to the dipoles in the $PbZr_{0.2}Ti_{0.8}O_3$ film. But the residue is still rather localized and therefore does not appear to compromise electrical transport in the graphene channel or coupling between its doping level and the ferroelectric polarization (compare Chapter 4).

Secondly, piezoresponse force microscopy (PFM) was employed to map the domain structures of the ferroelectric films and single crystals. PFM is a contact mode scan using electrically conductive AFM tips. It measures the mechanical response to an applied voltage, known as the piezoelectric effect. If an oscillating potential is applied to the tip, a ferroelectric material exhibits a mechanical response based on its polarization direction. Therefore, the phase difference between the electrical excitation and the mechanical response φ can be utilized to map the domain structure of a given ferroelectric. For down-polarized *c*-domains, the application of a positive tip bias results in the expansion of the sample, and surface oscillations are in phase with

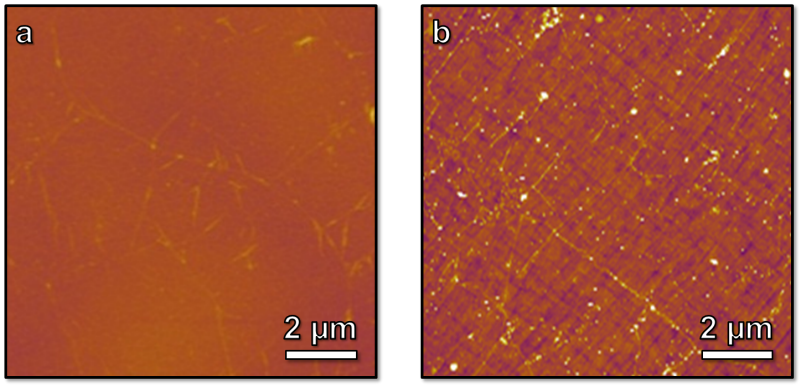

Figure 3.6: AFM topography images of graphene. a) Chemical vapor deposition grown graphene transferred to SiO_2 as a reference substrate. Negligible amounts of organic residue (small, white dots) and grain boundaries are visible (thin lines). b) Graphene transferred similarly to a $PbZr_{0.2}Ti_{0.8}O_3$ film. Underneath the graphene layer, the $PbZr_{0.2}Ti_{0.8}O_3$ domain structure is visible. A slightly higher, but still tolerable amount of organic residue is detected.

the tip voltage. For up-polarized c-domains, the response is opposite and $\varphi = 180°$. More details are given in ref. [59].

A PFM scan on a $PbZr_{0.2}Ti_{0.8}O_3$ film is presented in figure 3.7. The topography image (panel a) reveals an extremely smooth film with a root mean square roughness of less than 300 pm. The PFM phase and amplitude images (panels b and c) reveal that the film is mostly oriented in the same out-of-plane direction with a small fraction of a-domains visible in the amplitude image. Because of the sample orientation with respect to the AFM tip, these are visible as diagonal lines due to the difference in piezoresponse in different crystallographic directions. Both tapping mode topography and PFM imaging were performed on an Asylum Research Cypher AFM.

3.2.2 X-ray Diffraction

X-ray diffraction is a powerful tool to map the crystallographic characteristics of a given crystal. In the Philips X'Pert MRD system used for the analysis of the $PbZr_{0.2}Ti_{0.8}O_3$ thin films, the so-called Bragg-Bretano geometry is used. A beam $\vec{K}_i$ of Cu $K_{\alpha 1}$ radiation with $\lambda = 1.54059$ Å illuminates the sample under the angle θ.

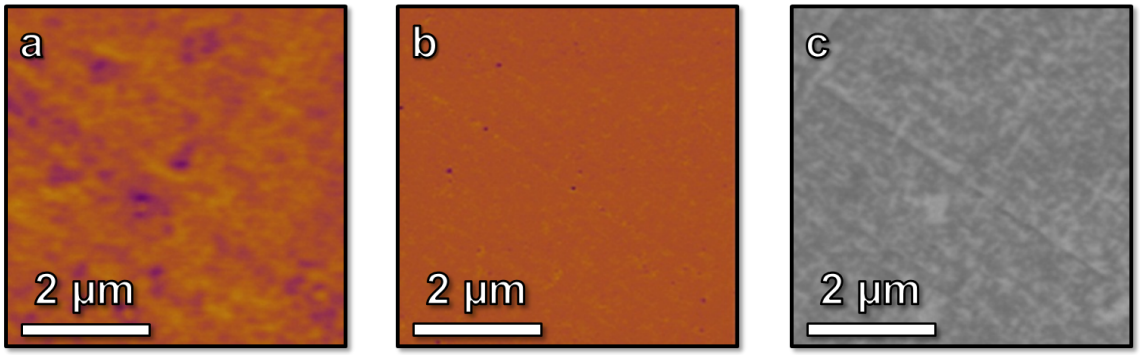

Figure 3.7: Scanning probe characterization of $PbZr_{0.2}Ti_{0.8}O_3$ films. a) Topography image. b) PFM phase image. Nearly the entire sample is polarized into the same out-of-plane direction. c) PFM amplitude image. A small fraction of a-domains is visible.

The scattered beam $\vec{K}_s$ is analyzed in the detector after passing the three-bounces-analyzer crystal.

X-ray scattering by crystal lattices can be most easily understood using the reciprocal space. A detectable x-ray scattering event always follows the Laue condition, i.e. the scattering vector $\vec{Q} = \vec{K}_s - \vec{K}_i$ must coincide with a reciprocal lattice vector $\vec{G}$. The peaks recorded in a diffraction pattern therefore correspond to a set of lattice planes (hkl). For a heteroepitaxial system, the reciprocal space lattice is a superimposition of the layer and substrate lattice. The detailed analysis of the position of film peaks with respect to the substrate peaks provides a powerful tool for the characterization of the crystal structure and orientation of thin films with respect to the substrate. More details can be found in [60].

The X-ray diffraction pattern depicted in figure 3.8 reveals that the puled laser deposition grown thin film heterostructures are indeed epitaxial and single phase, demonstrating the high crystal quality of the films.

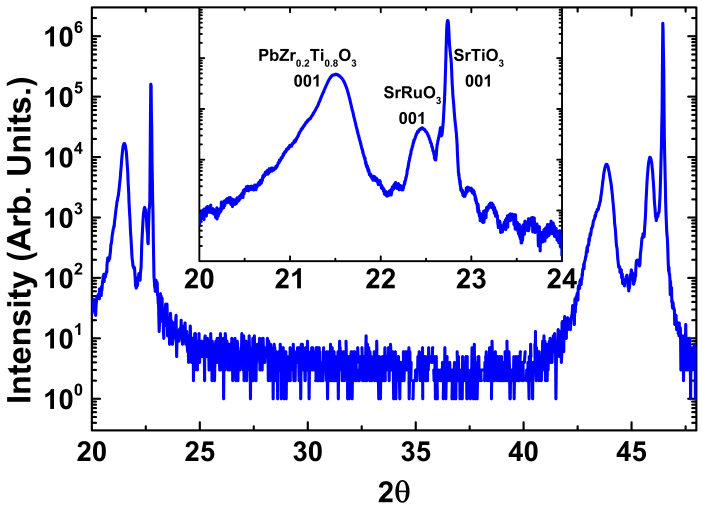

Figure 3.8: $\theta - 2\theta$ X-ray diffraction pattern about the 001- and 002-diffraction peaks for the $PbZr_{0.2}Ti_{0.8}O_3/SrRuO_3/SrTiO_3$ thin film heterostructure reveals single-phase, epitaxial film and bottom electrode.

3.2.3 Raman Spectroscopy

Raman Spectroscopy is a nondestructive characterization tool based on the detection of inelastically scattered light under laser illumination. The activation process for different peaks in the collected spectrum can be thought of in terms of the creation and recombination of a virtual electron-hole pair which exchanges momentum with phonons in one or several scattering events. A condition that the phonons have to fulfill in order to have a Raman signal is that the phonon modes belong to the same symmetry species as a component of polarizability [61]. Thus a sample dependent Raman active phonon spectrum can be collected, which allows for conclusions about electronic and thermal properties of graphene.

The particular phonon modes of importance for the Raman analysis of graphene are the in-plane longitudinal and transverse optical modes. The characteristic Raman spectrum for graphene [figure 3.9] consists of the G and 2D peaks at $\sim$1585 cm^{-1} and $\sim$2677 cm^{-1}, respectively, for an excitation with a laser of wavelength 532 nm and an essentially defect free graphene piece. If the graphene piece contains a high

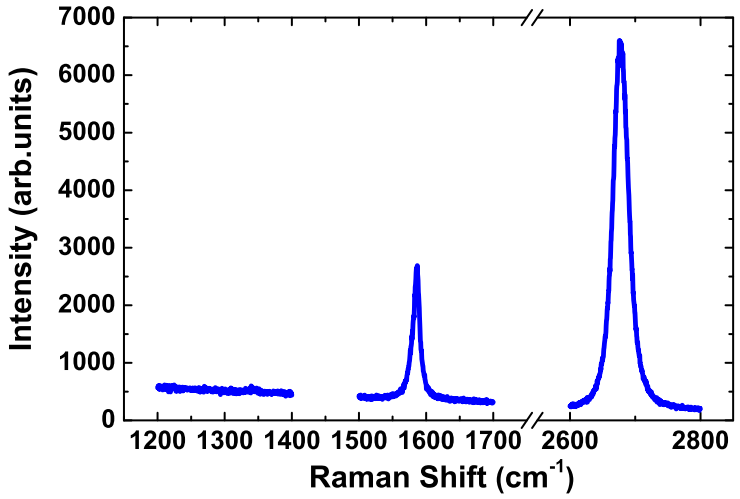

Figure 3.9: Raman spectrum of single-layer graphene grown *via* chemical vapor deposition and transferred to SiO_2. The absence of a D peak around 1340 cm^{-1} with $I(D)/I(G) < 3$ % reveals an extremely low defect density. The height ratio of about 3 between the 2D peak at around 2677 cm^{-1} and the G peak around 1585.6 cm^{-1} as well as the full width at half maximum of the 2D peak $\Gamma_{2D} = 26.8$ cm^{-1} confirm the monolayer thickness.

density of defects, the so-called D band at ∼1340 cm^{-1} become detectable because the mechanism causing this peak involves scattering of the virtual electron hole pair at defects.

The G band corresponds to the doubly degenerate E_{2g} phonon mode at the Brillouin zone center, the D and 2D bands involve scattering at the A_1' in-plane transverse optical mode (iTO) near the K point, which is the breathing mode of six-atom rings [62]. For the D band, the electron-hole pair is scattered at one of these phonons and one defect, while the 2D band originates from a second order scattering involving two phonons.

According to ref. [63], the concentration of point defects n_D in a given sample can be estimated by

$$n_D\left(\mathrm{cm}^{-2}\right) = \frac{(1.8 \pm 0.5) \times 10^{22}}{\lambda_{Laser}(\mathrm{nm})^4} \left(\frac{I_D}{I_G}\right) \tag{3.1}$$

with the laser wavelength λ_{Laser}, and the intensities I_D and I_G for the D and G peak, respectively. Using the intensity ratio $I(D)/I(G) < 3$ % of the chemical vapor deposition grown graphene in figure 3.9, the defect density in this sample is about 70 μm^{-2}, which corresponds to a very small fraction of about 70 point defects in an area containing 550,000 atoms.

Beyond establishing the crystalline quality, Raman spectroscopy contains extensive information about the doping level of graphene films. Because of the zero-bandgap nature of graphene, lattice vibrations are partially screened by conduction electrons, as the energy scales for electron and phonon dynamics are comparable. Therefore, the adiabatic Born-Oppenheimer approximation, which allows the separation of the wavefunction of a given molecule or crystal into electronic and nuclear components, fails in this case [64, 65]. At reciprocal points where the phonon wave vector $q = k_1 - k_2$, with k_1 and k_2 being wavevectors corresponding to electronic states on the Fermi level, the phonon dispersion contains a divergence, the so-called Kohn anomaly, which gives rise to very rapid change of the ability of the conduction electrons to screen the lattice vibrations [66]. Because of the 2-dimensional structure of graphene, the phonons associated with Kohn anomalies lie at the K and Γ points in the Brillouin zone, which are also giving rise to the Raman 2D- and G-bands [67].

The physical reason for the interaction between electrons and phonons lies in the fact that optical phonons distort the distance between neighboring carbon atoms. This effect changes the electronic band structure and can be quantified in terms of the electron-phonon-coupling matrix element (EPC). The renormalization due to EPC is strongest close to the Dirac point and leads to phonon softening (red shift of the G-band frequency) [figure 3.10] [68]. A slight asymmetry with respect to the Dirac point is expected theoretically because of the decrease (increase) of the C-C bond length due to the addition (reduction) of electrons to the antibonding orbitals [65].

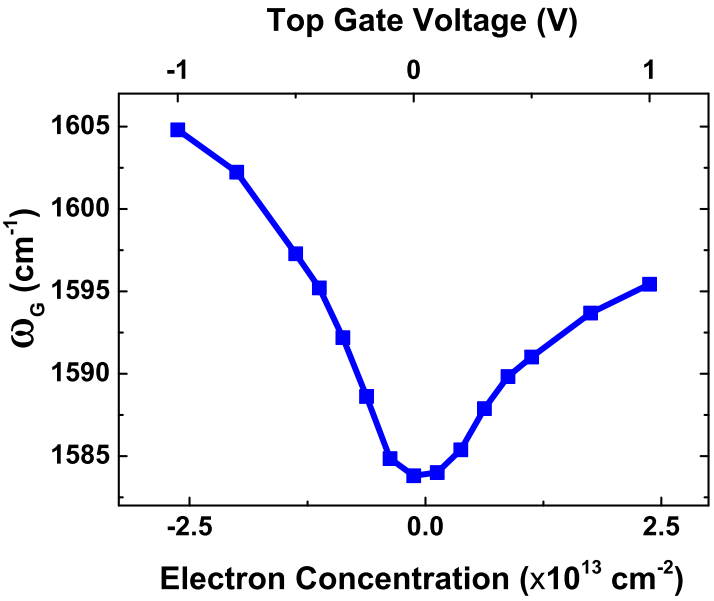

Figure 3.10: G-band frequency as a function of the carrier density. For this particular sample, graphene was transferred to an up-polarized $LiNbO_3$ crystal and top-gated with a PEO electrolyte. The electron concentration was calculated using the gating efficiency of the electrolyte derived in Chapter 5 and the applied top gate voltage.

For the 2D band, a frequency shift upon doping is expected and experimentally observed for similar reasons as for the G-band peak [65], but it is not expected to depend as strongly on the carrier concentration. The overall change of the 2D band frequency is much smaller than for the G-band ($\Delta\omega_{2D} \lesssim 2$ cm^{-1}) and rather close to experimental resolution. Instead of the peak position, the intensity and FWHM dependence on the doping level are of significant experimental importance. The intensity is strongly susceptible to the carrier concentration, while the FWHM is nearly constant, leading to a decrease in integrated area with increasing carrier concentration. The reason for the dispersive behavior of the integrated intensity lies in the fact that the peak intensity is proportional to the electron/hole scattering rate, which is increased by the increase of carrier concentration upon doping. The apparent contradiction to the constant integrated area of the G-band can be understood as the 2D-band two-phonon scattering event is fully resonant, so that the intermediate elec-

tron and hole states correspond to real particles, propagating along the quasiclassical trajectories and subject to scattering processes [62].

The understanding of the processes governing the Raman signal of a graphene layer can also be utilized to determine whether it is indeed a single layer. For chemical vapor deposition grown graphene, electronic coupling between each layer of few-layer graphite leads to significant broadening and reduction in intensity of the 2D peak. While a broadening of the peak can also be induced by defects and therefore yields no deterministic information about the thickness, the intensity ratio at a given doping level can clearly identify single-layer graphene [65]. The height ratio $I(2D)/I(G) > 3$ with $\omega_G = 1585.6$ cm^{-1} as well as the full width at half maximum of the 2D peak $\Gamma_{2D} = 26.8$ cm^{-1} confirm that the graphene grown as described in section 3.1.2 is indeed of monolayer thickness [figure 3.9].

Two dimensional Raman maps were acquired with a WITec Confocal Raman Microscope alpha300, single point spectra and experiments with electrically contacted or gated samples were performed on a Jobin Yvon Labram HR800 micro-Raman spectrometer. For both instruments, 532 nm laser excitation and 100× air objectives (laser spot size 1 µm) were used. The laser intensity is kept around 1 mW to ensure that laser-induced heating does not introduce artifacts. All peaks were fitted with a single Lorentzian. In the case of the spectra on $PbZr_{0.2}Ti_{0.8}O_3$ films, the background spectrum acquired next to the graphene channel was subtracted before fitting.

3.2.4 Electrical Characterization

The graphene/$PbZr_{0.2}Ti_{0.8}O_3$ capacitor structures were analyzed using a Radiant Technologies Multiferroic Tester. Leakage current measurements in the as-poled state as well as hysteresis loops at a frequency of 10 kHz were performed. Detailed Positive Up Negative Down (PUND) measurements were used to determine the switched polarization as a function of pulse width and applied voltage. This technique allows

ferroelectric characterization based on a series of five pulses. The initial pulse is used to preset the polarization state. No measurement is made after this pulse. A second pulse is applied and the switched polarization is detected. All non-remanent polarization is allowed to dissipate and the polarization is measured again. A third pulse of the same voltage as the second pulse is used to measure the non-remanent polarization. The difference of the measured values after the second and third pulses corresponds to the switchable and remanent polarization and is commonly reported to characterize a ferroelectric device. The fourth and fifth pulse repeat the measurement of the second and third pulse with opposite polarity. This routine is repeated for a range of pulse widths and voltages.

For the characterization of graphene/$PbZr_{0.2}Ti_{0.8}O_3$ FETs, an Agilent Semiconductor Parameter Analyzer 4155C was used, which allows for the simultaneous application and measurement of gate-, source- and drain-voltage as well as the corresponding currents through source measure units. The standard characterization for all FET structures used here was a gate-voltage sweep with a constant drain voltage of 50 mV with the source electrode held at ground. The sweep rate was carefully controlled through the delay before each voltage step and has been varied between 0.01 and 6.67 V/s.

The sample preparation and characterization presented in this chapter provide the basis for the development and utilization of graphene/ferroelectric hybrid structures. As will be shown below, favorable device characteristics and promising spatial control of the graphene doping level result from the combination of these material classes.

Chapter 4

Tunable Carrier Density and Type in Graphene/$PbZr_{0.2}Ti_{0.8}O_3$ Hybrid Structures through Ferroelectric Switching[1]

In this chapter, reversible and permanent switching of the ferroelectric polarization in graphene/$PbZr_{0.2}Ti_{0.8}O_3$ capacitors and FETs is demonstrated. The switching of the polarization direction during the FET operation results in a reversal of the usually observed hysteresis direction when external environmental factors are minimized. The conversion of p-type graphene into n-type with an estimated carrier density change as large as $\sim 10^{13}$ cm^{-2} is demonstrated.

4.1 Ferroelectric Switching in Capacitor and Transistor Devices

The Pd/graphene/$PbZr_{0.2}Ti_{0.8}O_3$/$SrRuO_3$ capacitors, which were fabricated as discussed in section 3.1.4, show symmetric and low leakage current compared to contacts involving a common wetting layer such as Cr or Ti [figure 4.1a] [54, 55]. This is caused by the high crystal quality of the film and similar work functions of the top- and bottom electrodes. Because of the low leakage, ferroelectric hysteresis loops can be easily detected. Unlike previous reports on graphene/$PbZr_{0.2}Ti_{0.8}O_3$ hybrid devices, which have not yet revealed ferroelectric switching with graphene

[1] A large portion of the information presented in this chapter has been adapted with permission from C. Baeumer *et al.,* Tunable Carrier Type and Density in Graphene/$PbZr_{0.2}Ti_{0.8}O_3$ Hybrid Structures through Ferroelectric Switching, *Nano Letters* **13** (2013). Doi 10.1021/nl4002052. Copyright (2013) American Chemical Society.

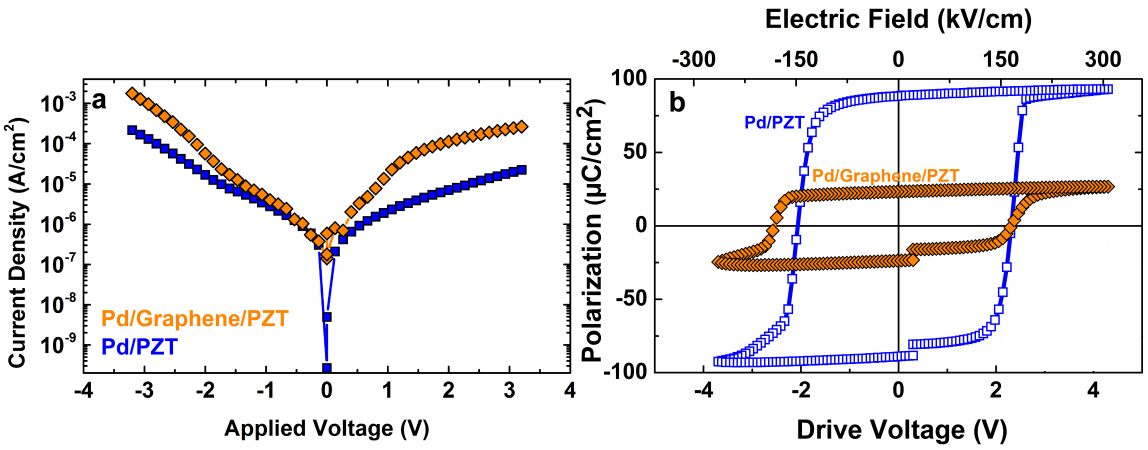

Figure 4.1: a) Leakage current for representative capacitors with Pd (blue squares) and Graphene/Pd (orange diamonds) top contacts. In both cases, the leakage is reasonably low and symmetric. The reason no switching currents are detected near the coercive voltages is that the capacitors are poled in the direction of measurement prior to the application of positive or negative voltages. b) Ferroelectric hysteresis loops of the $PbZr_{0.2}Ti_{0.8}O_3$ (PZT) film with Pd and graphene/Pd top contacts (blue, open squares and orange, filled diamonds, respectively) with a frequency of 10 kHz.

contacts, a robust ferroelectric response of the $PbZr_{0.2}Ti_{0.8}O_3$ film can be seen in the Pd/graphene/$PbZr_{0.2}Ti_{0.8}O_3$/$SrRuO_3$ capacitors with a coercive field of $\sim$174 kV·cm^{-1} ($\sim$2.44 V coercive voltage) [figure 4.1b]. As a point of comparison, the hysteresis loop for a Pd top contact capacitor without graphene is also shown [figure 4.1a and b]. Symmetric leakage current, square and symmetric hysteresis loops, negligible polarization offsets, and similar coercive fields are seen in the control capacitor.

A noticeable difference is the smaller remanent polarization of the Pd/graphene/$PbZr_{0.2}Ti_{0.8}O_3$ structures ($\sim$23 μC·cm^{-2} vs. $\sim$80 μC·cm^{-2} in the control), which can be explained by the lower carrier density of the graphene being unable to compensate the polarization completely, leading to a significant depolarization field, which decreases the polarization as described in section 2.2. A complete compensation of the remanent polarization would require a carrier density of about 5×10^{14} cm^2, an enormous number for single-layer graphene. Graphene

covered by a ferroelectric polymer film has also been shown to be unable to supply a sufficient number of carriers for complete compensation [26]. Another possible explanation for the reduced polarization is the existence of a dielectric layer at the interface of the graphene and $PbZr_{0.2}Ti_{0.8}O_3$ films, possibly caused by molecules such as H_2O present on the surface of the $PbZr_{0.2}Ti_{0.8}O_3$ prior to or during the transfer process.

The voltage magnitude and the pulse-width dependent results obtained using PUND measurements of $PbZr_{0.2}Ti_{0.8}O_3$ capacitors with Pd/graphene contacts are shown in figure 4.2. Fast ferroelectric polarization switching can be achieved in these capacitors. For a complete polarization reversal, pulse durations of 0.008 ms, 0.032 ms and 0.51 ms are required for applied voltages of ± 3.5 V, ± 3 V and ± 2.5 V, respectively. These results provide the necessary information to understand the time- and gate-voltage-dependent response of graphene FETs on $PbZr_{0.2}Ti_{0.8}O_3$. Fast and low-voltage responses may be particularly useful for manipulating electron transport in graphene with ferroelectric gates.

Having established fast and robust ferroelectric polarization switching of $PbZr_{0.2}Ti_{0.8}O_3$ using graphene-based electrodes, a similar switching characteristic is expected in a FET geometry with a graphene channel and a ferroelectric gate. For gate voltages not exceeding the coercive voltage of the $PbZr_{0.2}Ti_{0.8}O_3$ film, these devices [see section 3.1.4] exhibit transfer characteristics similar to graphene FETs on Si/SiO_2 substrates, further verified through gate-dependent Raman G-band peak position shift [figure 4.3]. Due to the large dielectric constant of $PbZr_{0.2}Ti_{0.8}O_3$, a very small V_G range is necessary to effectively tune the carrier concentration. The Dirac point is typically at a slightly positive V_G (i.e., p-doped much like graphene on Si/SiO_2 substrates measured under air ambient) and the field-effect mobility is in the range of 200 to 1,300 $cm^2V^{-1}s^{-1}$. The similarity between the forward and backward sweep confirms that there is only a small fraction of extrinsic hysteresis for small gate

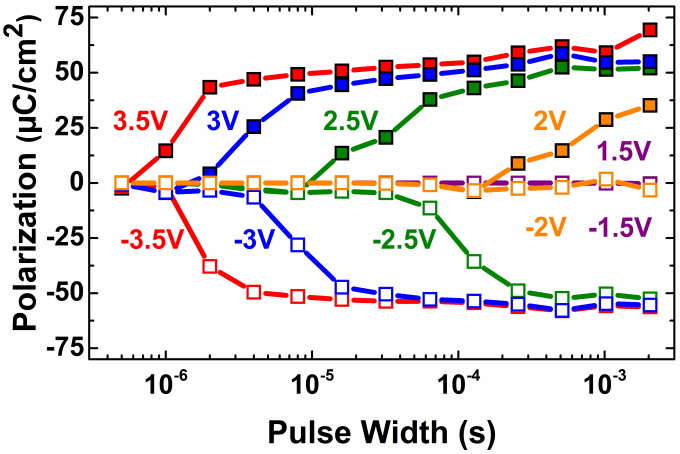

Figure 4.2: PUND (Positve Up Negative Down) switching measurements for a Pd/-graphene/ $PbZr_{0.2}Ti_{0.8}O_3$ capacitor as a function of pulse width for various pulse voltages. The ferroelectric polarization can be switched completely for positive and negative voltages with pulse durations of 0.008 ms, 0.032 ms and 0.51 ms for applied voltages of ± 3.5 V, ± 3 V and ± 2.5 V, respectively.

voltage ranges. This is distinctly different from previous results obtained with similar structures and will be discussed in more detail in section 4.2.

A more complex behavior is observed when V_G exceeds the coercive field [figure 4.4a]. Starting from $V_G = -5$ V, which causes the $PbZr_{0.2}Ti_{0.8}O_3$ to be poled "down" (i.e., polarization direction shown in the upper left inset of figure 4.4b), sweeping V_G towards more positive values with a relatively slow sweep rate of 0.0187 V/s for this particular case reveals that the drain current (I_D) of this device reaches a minimum at $V_G = 1.36$ V, the Dirac point. As V_G becomes more positive, I_D starts to deviate from the "V-shape" of ambipolar behavior expected for a graphene FET with non-ferroelectric gate dielectric. At $V_G \approx 2.5$ V, I_D shows a pronounced maximum followed by a strong decrease. In the reverse sweep, the Dirac point lies at $\sim$3.4 V. This shift in the Dirac point is indicative of strongly enhanced p-doping. At $V_G \approx 2.5$ V, another maximum followed by a rapid decrease in I_D is observed. Given that these non-monotonic points in the I_D-V_G characteristics at $V_G \approx \pm 2.5$ V match

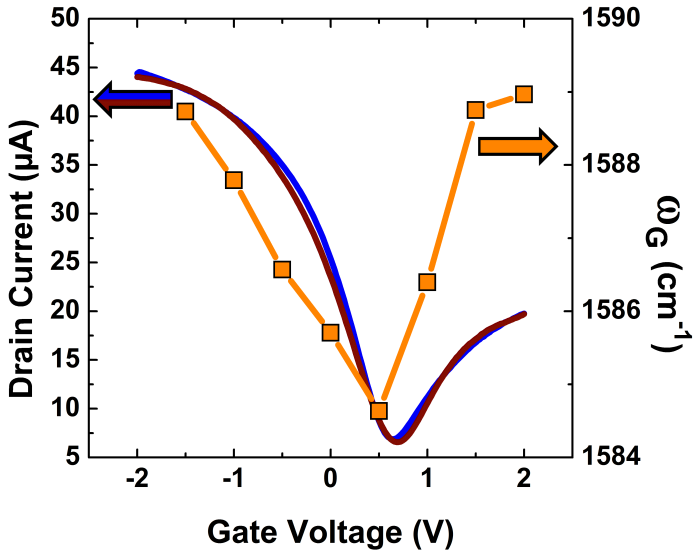

Figure 4.3: Representative gate dependent drain current (blue solid line and red solid line for forward and reverse sweep, respectively) and Raman G-peak position (orange squares) for small gate voltage sweeps in the as-grown state.

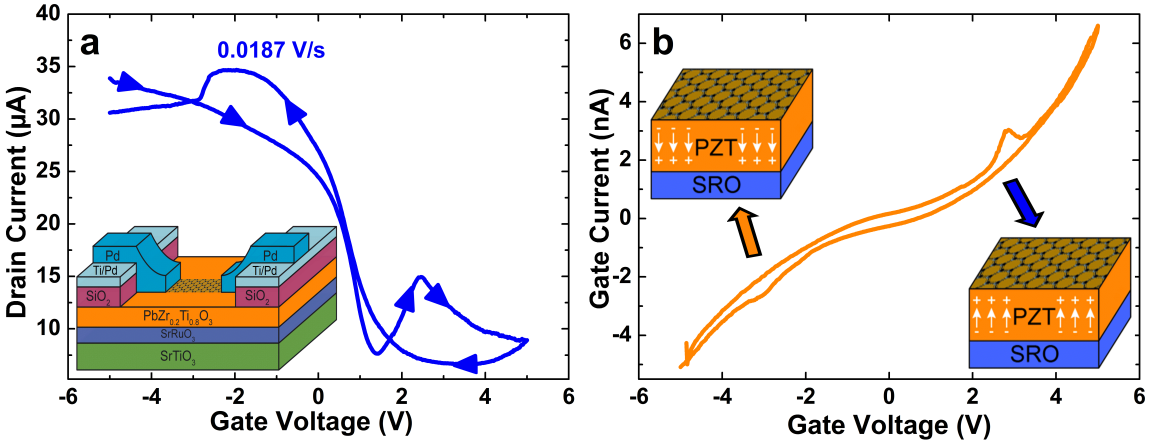

Figure 4.4: a) Complex I_D-V_G-characteristic for large gate voltages with a drain voltage of 50 mV and a gate voltage sweep rate of 0.0187 V/s. Inset: Schematic of a graphene transistor on $PbZr_{0.2}Ti_{0.8}O_3$. b) Gate current measured simultaneously to (a). Note the different scales for drain and gate current. The gate current was always equal or less than 0.1 % of the drain current. Insets: Schematics of the ferroelectric polarization for different gate voltage regimes.

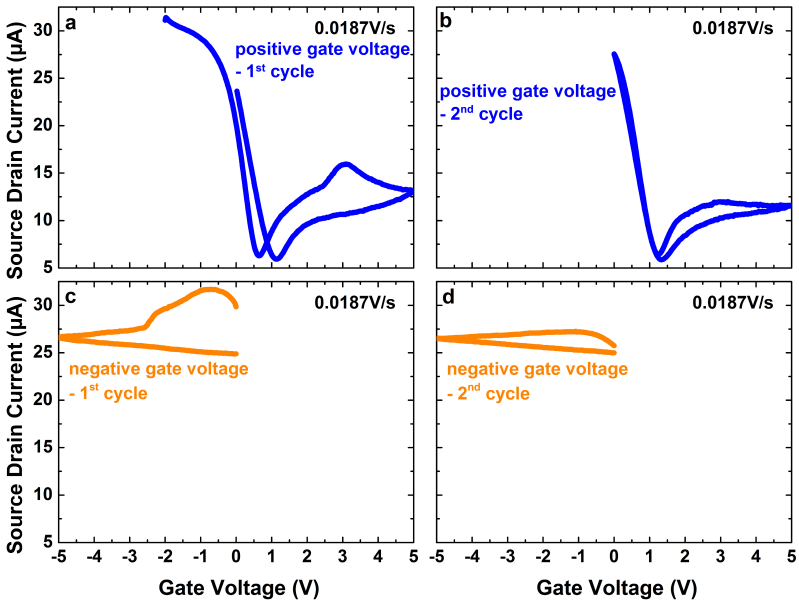

Figure 4.5: Repeated gate voltage sweeps in the same direction with a sweep rate of 0.0187 V/s for positive (a and b) and negative (c and d) gate voltages.

the independently determined coercive fields of $PbZr_{0.2}Ti_{0.8}O_3$, it appears that the polarization reversal in the ferroelectric film is responsible for the sudden drops in I_D and the shift in the Dirac point.

This conclusion is further validated in the gate leakage current (I_G) behavior [figure 4.4b] where precisely at the non-monotonic points in I_D (at $V_G = \pm 2.5$ V) there are increases in $|I_G|$ corresponding to the polarization switching up (down) for positive (negative) V_G. These results are also similar to the recently observed I_G response of carbon nanotube network transistors with ferroelectric polymer gate insulators [69]. Additionally, multiple sweeps in the same direction further confirm that the polarization reversal is the cause of the non-monotonic behavior [figure 4.5]. That is, once the polarization of $PbZr_{0.2}Ti_{0.8}O_3$ has been switched, applying the same switching voltage will not lead to observation of another maximum in I_D or $|I_G|$. In other words, starting with "down" poled $PbZr_{0.2}Ti_{0.8}O_3$, sweeping V_G from 0 to +5 V for the first time will show maxima in I_D and I_G at $V_G = \pm 2.5$ V but sweeping additional times from 0 to +5 V will not result in the same maxima at $V_G = \pm 2.5$ V.

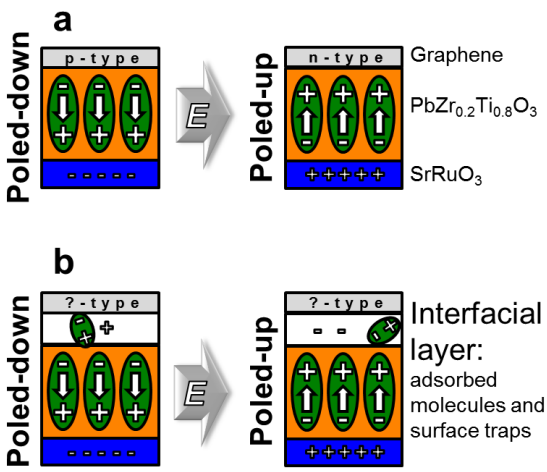

Figure 4.6: Schematic of the switching process in graphene/PZT hybrid devices. a) Ideal behavior. b) Suggested mechanism for the observed phenomena.

4.2 Minimizing Extrinsic Hysteresis Effects

While the simultaneous rise in $|I_G|$ with the drop in I_D [figure 4.4] is expected at the coercive voltages where the reversal of ferroelectric polarization occurs, the direction of the shift of the Dirac point and therefore the direction of the hysteresis requires further consideration. Enhanced p-doping (positive shift of the Dirac point) upon switching the polarization up with positive V_G is in agreement with previous experimental results for graphene [20, 21] and CNT [70] based ferroelectric hybrid devices. This hysteresis, however, cannot be caused directly by the ferroelectric polarization and therefore must be explained by extrinsic effects including charging and dipole screening effects likely associated with adsorbed molecules at the interface. If the graphene doping level coupled directly to the polarization, it would shift from p-type to n-type upon the application of positive gate voltages [figure 4.6a]. Only the existence of charge traps and adsorbed molecules can account for the experimental observation, as is depicted schematically in figure 4.6b.

This interpretation is experimentally supported in two ways. The first set of evidence comes from the changing behavior of graphene with V_G sweep rate. Transfer

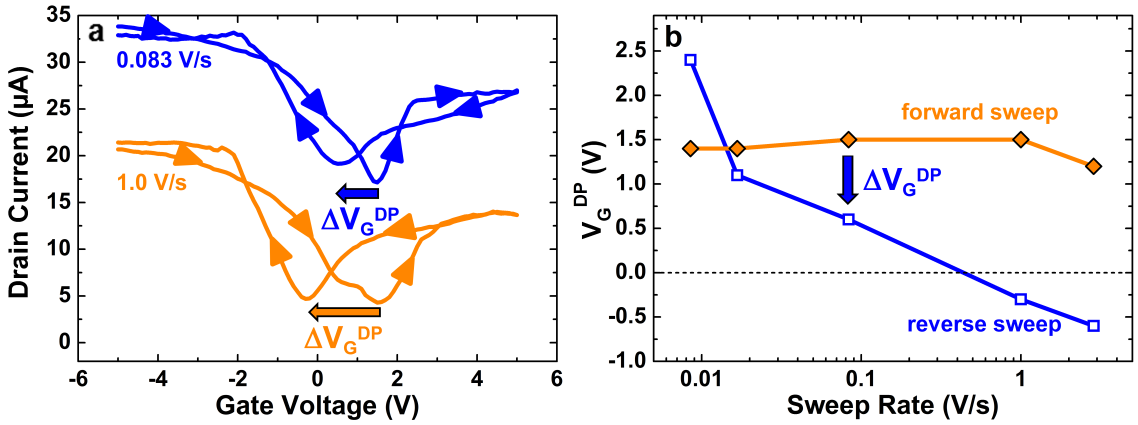

Figure 4.7: a) Complex I_D-V_G characteristics of another graphene/ $PbZr_{0.2}Ti_{0.8}O_3$ transistor for gate voltage sweeps past the $PbZr_{0.2}Ti_{0.8}O_3$ coercive voltage for two representative sweep rates as indicated. b) Sweep-rate dependent position of the current minima defined as the Dirac point voltage V_G^{DP} in the forward (orange, filled diamonds) and reverse sweep (blue, open squares). The dotted line represents zero gate voltage and separates the regimes of n- and p-doping.

characteristics reveal that faster sweep rates actually cause a reduction in the p-doping of the graphene and can even lead to n-doping as shown for the case of the sweep rate =1 V/s [figure 4.7a]. The V_G sweep rate dependence of the Dirac point shift (ΔV_G^{DP}) [figure 4.7b] may then be explained by time-dependent charging/discharging or charge redistribution effects at the graphene/$PbZr_{0.2}Ti_{0.8}O_3$ interface. For non-ferroelectric gate dielectrics, increasing V_G sweep rate can only reduce the hysteresis associated with the positive ΔV_G^{DP} [40]. This is a distinctly different behavior than that observed for graphene on the ferroelectric $PbZr_{0.2}Ti_{0.8}O_3$ gate where the hysteresis is first transposed to the reverse direction, then the magnitude of the hysteresis increases with further increase in sweep rate.

The second set of evidence for extrinsic charging/molecular adsorption effects complicating the observed hysteresis in the transfer curves of graphene FETs on $PbZr_{0.2}Ti_{0.8}O_3$ lies in the spatial inhomogeneity of charge distribution. Switching the polarization of $PbZr_{0.2}Ti_{0.8}O_3$ from "down" to "up" poled at a sweep rate of 0.046 V/s leads to a reduction in p-doping as verified by the net decrease in Raman G-band

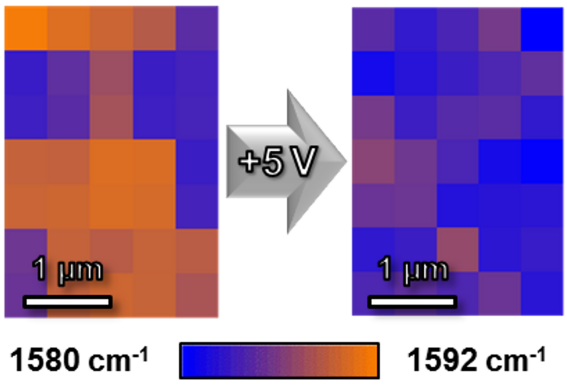

Figure 4.8: Raman G-band frequency maps for a graphene transistor after gate sweeps ending at -5 V (left) and +5 V (right) with a gate voltage sweep rate of 0.046 V/s.

position to a nearly intrinsic level [figure 4.8c]. More detailed examination of the Raman maps reveals local variations in the G-band position for both the "up" and "down" poled cases, which are indicatives of charge inhomogeneities. These variations in charge density are reminiscent of "charge puddles" that have been associated with spatial distribution of the surface potential on non-ferroelectric substrates supporting the graphene layer [71,72]. This spatial inhomogeneity also manifests itself in a small, plateau-like shoulder in the transfer curves close to the Dirac point resulting from different regions of the graphene channel reaching minimum conductance at different gate voltages [forward sweep in the bottom curve in figure 4.7a for $V_G \approx 1$ V]. Similar behavior in the transfer characteristics has been shown to arise when local doping levels have been intentionally varied by charge injection into graphene/oxide interface trap states in a previous study [73]. Therefore, the observed complex hysteresis can be completely understood when the interface between the ferroelectric and the graphene channel is considered.

The importance of the interface between the $PbZr_{0.2}Ti_{0.8}O_3$ film and the graphene channel is emphasized further when the results of two different graphene transfer methods are compared. FET devices fabricated on a graphene/$PbZr_{0.2}Ti_{0.8}O_3$ hybrid structure created through the one-touch transfer method developed here were

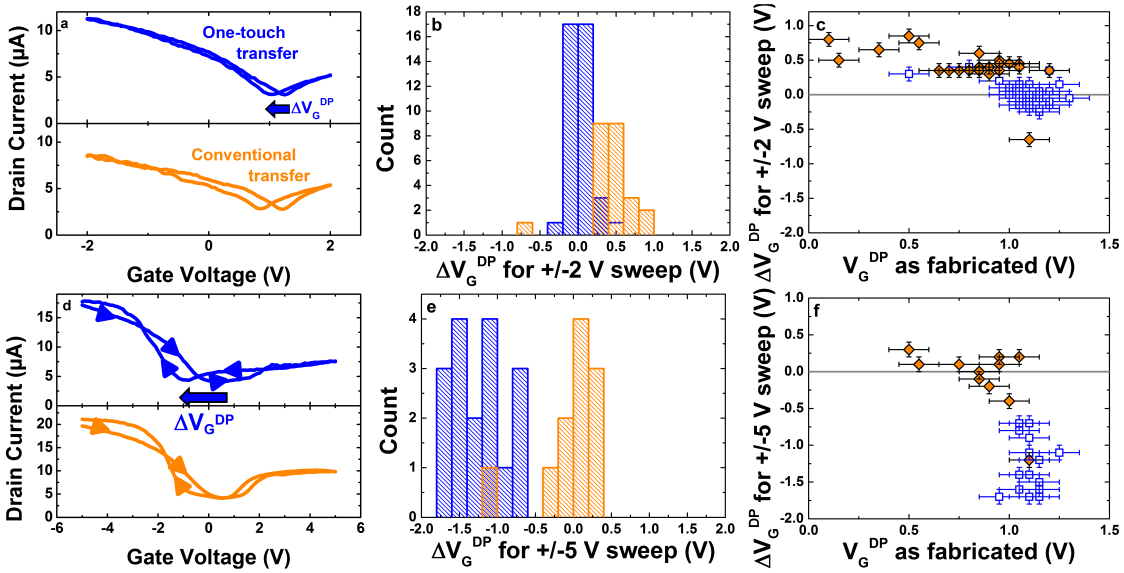

Figure 4.9: Comparison of devices fabricated using the "one-touch" transfer (blue columns, squares and lines) and the "conventional" transfer (orange columns, diamonds and lines). a) Representative small gate voltage sweeps below the coercive field for both transfer methods. b) Distribution of Dirac point shift ΔV_G^{DP} for small gate voltage sweeps. c) Dirac point shift (ΔV_G^{DP}) for small gate voltage sweeps as a function of the initial Dirac point (V_G^{DP} as-fabricated). d) Representative gate voltage sweeps exceeding the $PbZr_{0.2}Ti_{0.8}O_3$ coercive voltage. e) Distribution of ΔV_G^{DP} for gate voltage sweeps exceeding the coercive field. f) ΔV_G^{DP} for gate voltage sweeps exceeding the coercive field as a function of V_G^{DP} as-fabricated.

compared to devices on graphene/$PbZr_{0.2}Ti_{0.8}O_3$ structures fabricated through the more conventional transfer process [8]. This conventional process differed in that instead of a continuous flow of de-ionized water after Cu etching, the graphene/PMMA stack was transferred from the etching solution onto de-ionized water using a clean Si/SiO_2 wafer and allowed to float on the water for 10 minutes. Afterwards, the stack was deposited onto a $PbZr_{0.2}Ti_{0.8}O_3$ film by raising the substrate from below. The subsequent PMMA removal and device fabrication procedures remained unchanged.

For comparison, two graphene/$PbZr_{0.2}Ti_{0.8}O_3$ hybrid structures were fabricated using the two transfer methods using two $PbZr_{0.2}Ti_{0.8}O_3/SrRuO_3/SrTiO_3$ samples fabricated simultaneously. All cleaning and photolithography steps were then carried out in parallel. The transfer characteristics for both samples were compared for small gate voltages not exceeding the coercive field and larger voltages leading to ferroelectric switching [figure 4.9]. The representative transfer curves are shown in figure 4.9a for small gate voltage sweeps below the $PbZr_{0.2}Ti_{0.8}O_3$ coercive voltage. Devices fabricated using the one-touch method showed negligible hysteresis, as determined by the Dirac point voltage difference in the forward and reverse sweeps (ΔV_G^{DP}), with an average shift of $+0.014 \pm 0.15$ V for 39 devices [figure 4.9b]. Devices fabricated using the conventional transfer method showed a strongly enhanced hysteresis without ferroelectric switching, with an average shift of $+0.42 \pm 0.28$ V for 24 devices. This enhanced hysteresis can be explained by charging effects at the interface, suggesting a less favorable interface for direct interaction between the ferroelectric polarization and charge carriers in graphene when the conventional transfer method was used. ΔV_G^{DP} plotted as a function of the Dirac point voltage in the as-fabricated state (V_G^{DP}) also reveals a narrower distribution of the initial Dirac point for devices fabricated using the one-touch method [figure 4.9c].

The more favorable interface achieved through the one-touch transfer method becomes more pronounced with relatively fast (6.67 V/s) gate voltage sweep exceeding

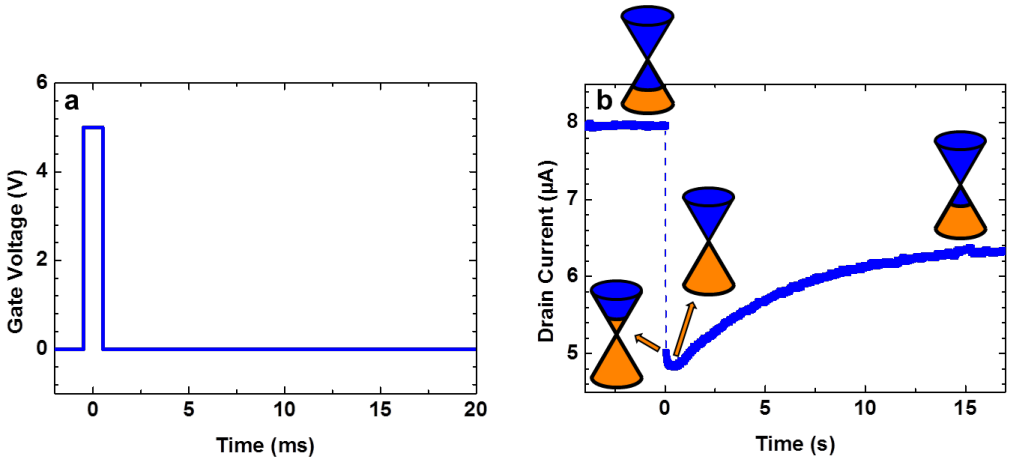

Figure 4.10: a) Applied gate voltage pulse. b) Current evolution before and after a 1 ms gate voltage pulse shown in a). The source-drain-current goes through a minimum corresponding to the Dirac point for this particular device before reaching a new equilibrium state. The current is monitored through integration over 40 ms for each data point, making the pure gate-effect during the pulse indiscernible.

the coercive voltage [figure 4.9d-e]. While a shift towards negative Dirac point voltages can be achieved for the one-touch method, with an average shift of -1.28 ± 0.36 V for 17 devices, the devices fabricated using the conventional transfer method showed close to zero average shift of the Dirac point (-0.082 ± 0.42 V). These results demonstrate the importance of a clean graphene/$PbZr_{0.2}Ti_{0.8}O_3$ interface in order for the ferroelectric polarization to have a direct observable impact on charge carriers in graphene.

Given that both ferroelectric polarization and variations in local charge density through interface traps and adsorbed molecules contribute to the observed ferroelectric-gated graphene FET characteristics, the time evolution of I_D upon polarization switching using a voltage pulse allows for further insight into the doping effects. In figure 4.10 the polarization of the $PbZr_{0.2}Ti_{0.8}O_3$ film is reversed using a short V_G pulse while I_D is monitored at a small applied drain voltage V_D of 50 mV. A 1 ms V_G pulse is applied at $t = 0$ and a sufficiently large voltage (5 V) is used to ensure complete switching of the polarization. Prior to the switching event, the graphene

exhibits a constant resistance, it is in a p-type state. Following the gate pulse, I_D drops instantaneously. Based on the sweep-rate dependence (compare figure 4.7), the graphene is expected to be slightly n-type at this stage. After the initial fast drop, I_D shows a slower response going through a minimum corresponding to the Dirac point at $t \approx 0.5$ s and then increasing to reach an equilibrium value. The final value of I_D corresponds to a net reduction in p-doping of the graphene with respect to the initial state. While the initial fast I_D drop is mainly in response to the ferroelectric polarization change, the switching event can also cause polar molecules adsorbed on the surface to rearrange to the altered local electric field or cause adsorption/desorption events. Then, the slow recovery of graphene towards p-type may be caused by the slow reconfiguration of polar molecules at the interface which can 1) partially screen the polarization field of the ferroelectric and 2) cause charge redistribution between graphene, adsorbed molecules and/or interface trap states. Despite the opposing slow molecular/interface effects, the final switched state of graphene remains non-volatile as discussed in section 4.3.

If the above hypothesis of adsorbed polar molecules causing the slow response that counteracts the direct effect of the ferroelectric polarization is correct, then varying the number of such molecules along with the ferroelectric polarization should allow a broader range of carrier densities (and type) in graphene to be accessible. To demonstrate this ability, the response of graphene FETs is measured in air and in vacuum ($< 3 \times 10^{-7}$ Torr) after annealing at 110 °C for several hours to reduce the number of adsorbed molecules. Figure 4.11b shows the transfer characteristics of a graphene FET under different conditions. These curves were measured within a small gate voltage range, well below the coercive voltage of the $PbZr_{0.2}Ti_{0.8}O_3$ film, after 1 ms gate voltage pulses to switch the ferroelectric polarization, as demonstrated in figure 4.11a. After a -5 V pulse in air, switching the polarization down, the graphene is p-doped with the Dirac point at $V_G \approx 1$ V. The positive value of the Dirac point and therefore

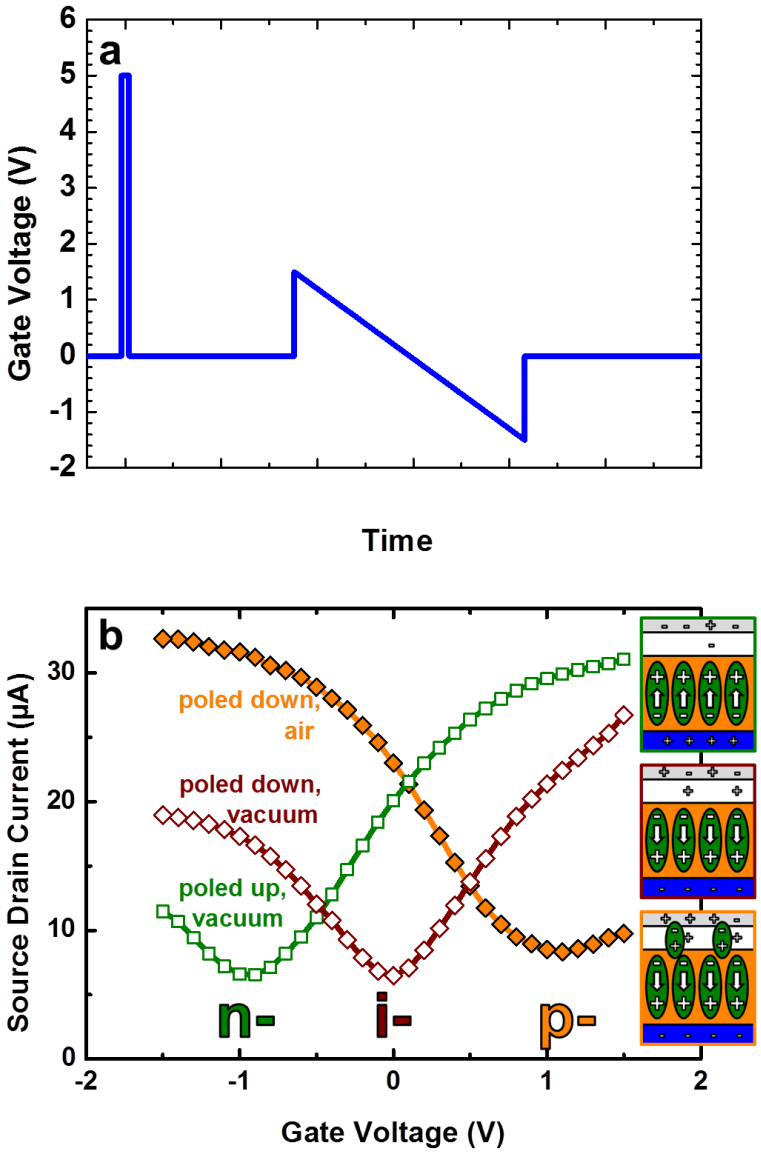

Figure 4.11: a) Gate voltage used to characterize graphene/PZT transistors in different environments with different polarization states. The polarization is switched into the desired state using a 1 ms gate voltage pulse of 5 V magnitude. Depicted here is the case of switching the polarization up. Subsequently, the graphene is characterized with a gate voltage sweep well below the coercive voltage. b) Small gate voltage sweeps in different environments and polarization states. p-type, nearly intrinsic, and n-type behavior can be observed after a -5 V pulse in air (orange, filled diamonds), a -5 V pulse in vacuum (red, open diamonds), and a +5 V pulse in vacuum (green, open squares), respectively.

the graphene being p-type can be attributed to a combination of doping due to the ferroelectric polarization, extrinsic effects of polar molecules, and charge trapping in the interface states. Performing the same operation in vacuum, the graphene channel is now nearly intrinsic (Dirac point at $V_G \approx 0$ V), which has to be attributed to the combination of the ferroelectric polarization and interfacial trap states after the (partial) removal of polar molecules through the vacuum heat treatment. A positive 5 V V_G pulse in vacuum, switching the polarization up, completely converts the graphene to n-type (Dirac point at $V_G \approx -1$ V), demonstrating that the switching of the ferroelectric polarization, rather than extrinsic effects of adsorbed molecules, dictate the carrier type and density. The different contributions leading to the detected doping levels are depicted in the cartoon images in figure 4.11b. The shift in the Dirac point from $V_G = 1$ V on a down-polarized $PbZr_{0.2}Ti_{0.8}O_3$ film in air to $V_G = -1$ V on an up-polarized $PbZr_{0.2}Ti_{0.8}O_3$ film in vacuum corresponds to an impressively large change in carrier density/type from $\sim 6 \times 10^{12}$ holes/cm^2 to $\sim 6 \times 10^{12}$ electrons/cm^2.

4.3 Device Operation Utilizing Tunable Carrier Type and Density

While the previous chapters introduced the fabrication and characterization of first generation graphene/$PbZr_{0.2}Ti_{0.8}O_3$ hybrid transistors, the understanding gained through the detailed analysis in section 4.2 can now be used to operate these devices as non-volatile transistors.

Figure 4.12 depicts the current evolution over an extended period of time after a switching event similar to the device shown in figure 4.10. Again, an initial fast drop in I_D is detected, corresponding to the graphene switching from p-type to nearly intrinsic or slightly n-type. After equilibration as discussed previously, the device remains in a slightly p-type state, which is easily distinguishable from the initial (poled-down)

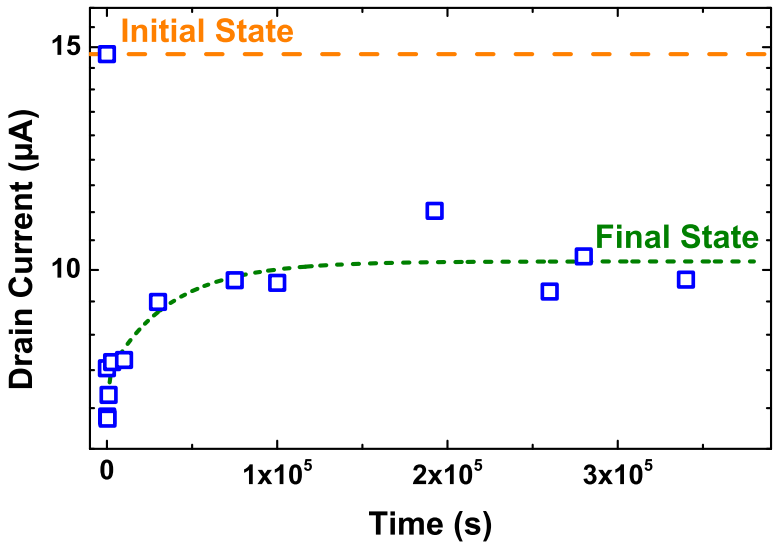

Figure 4.12: Retention measurement for a graphene transistor on $PbZr_{0.2}Ti_{0.8}O_3$. The drain current of a device switching between p-type and nearly intrinsic are monitored as a function of time after the switching event using a 1 ms pulse of 5 V magnitude, switching the polarization up (open, blue squares). The orange and green dashed lines correspond to the initial, p-doped state and a guide to the eye for the relaxation to a less p-type state, respectively. For each data point, the drain current is averaged over 50 s.

state. The non-volatile behavior exceeding 3×10^5 s is at least comparable with the current state of the art of ferroelectric FETs involving silicon, which similarly suffer from screening of the polarization by interface charge trapping [74].

In order to be an operable, non-volatile switch, the graphene/$PbZr_{0.2}Ti_{0.8}O_3$ transistors also need to exhibit completely reversible resistance states and fast switching speeds with low voltages are highly desirable. As depicted in figure 4.13, repeating the same switching operation multiple times in both directions yields highly repeatable response in the graphene resistance. Switching cycles of multiple thousand switches have been performed without lost of repeatability. The same operation can be performed in vacuum, demonstrating that switching between n-type and intrinsic in vacuum and p-type and intrinsic in air is accessible. Isolating the graphene channel from the surrounding environment with an n-type dopant like Poly(ethylenimine) (PEI) can lead to switching between different levels of n-type or nearly intrinsic lev-

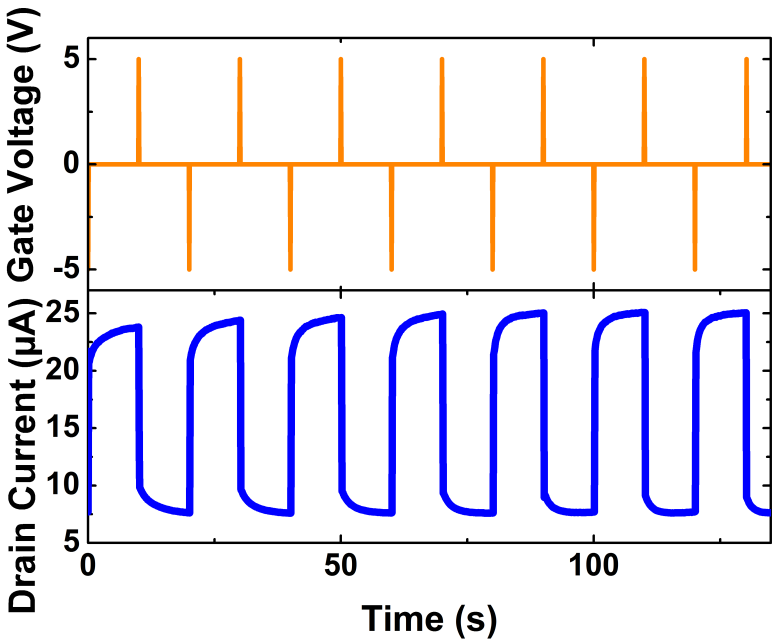

Figure 4.13: Multiple gate voltage pulses applied to a graphene/$PbZr_{0.2}Ti_{0.8}O_3$ FET in air (upper panel) and resulting reversible and reproducible switching between a highly p-doped state for the down-polarized state and a nearly intrinsic level for the up-polarized case (lower panel). The current is monitored through integration over 100 ms for each data point, making the pure gate-effect during the pulse indiscernible.

els as well, providing the accessibility to choose the carrier type even in ambient environments.

Repeatable and fast low voltage operation is demonstrated in figure 4.14. The drain current after polarization reversal is depicted for different pulse widths and voltages [figure 4.14a]. For voltages of ±6 V, operation in the μs regime is possible and switching between high- and low resistance states can be achieved down to 2 V. The operation with different pulse widths is also highly repeatable [figure 4.14b]. After the initial switching cycle, constant response to an applied voltage pulse is measured.

The device characteristics summarized in this chapter reveal the great potential of graphene/ferroelectric hybrid structures for future nanoelectronic devices. Bidirectional interdependency between the graphene doping level and the ferroelectric polarization indeed exists and results in ferroelectric FETs exhibiting highly

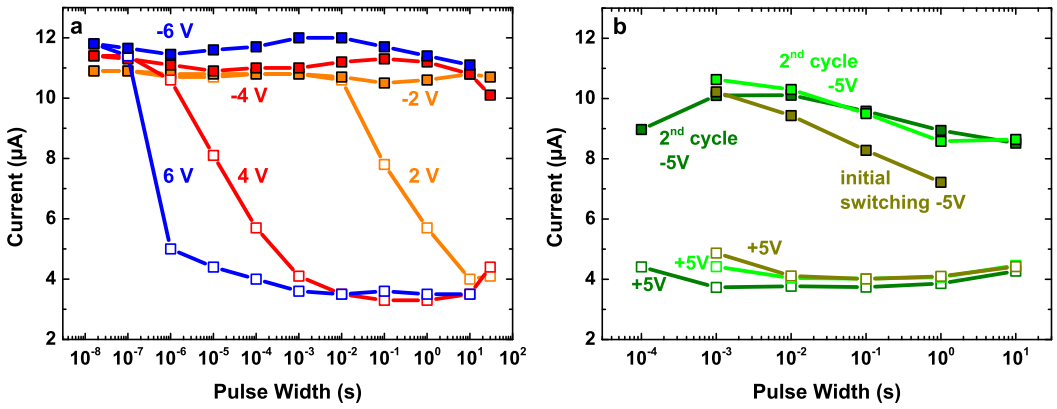

Figure 4.14: Low voltage operation. a) Drain current of a graphene transistor measured after a gate voltage pulse as a function of pulse width for different voltages. Complete and reversible switching between the "p" and "i" case can be achieved for 10^{-6} s, 10^{-3} s and 10 s for applied voltages of ± 6 V, ± 4 V and ± 2 V. Note the remarkable qualitative similarity between the switching of the doping level in the graphene channel and the ferroelectric polarization reversal provided in figure 4.2. b) Repeatability of the resistance change for different pulse widths for 5 V pulses for a similar device.

desirable fast and low-voltage response and non-volatile behavior. Notwithstanding, the low on-off ratio generally observed in graphene FETs is not yet overcome. Therefore, the applicability of graphene transistors on polydomain ferroelectrics is analyzed to provide a materials basis to overcome this challenge through the development of more sophisticated devices for complex carrier manipulation.

Chapter 5

Ferroelectrically Induced Spatial Carrier Density Modulation in Graphene

In this chapter, the spatial control of the carrier density through the underlying ferroelectric domain structure is presented. Graphene on periodically poled $LiNbO_3$ was used to demonstrate that graphene transferred to polydomain ferroelectrics exhibits a spatial density modulation corresponding to the domain structure. A detailed analysis revealed that similar to the ferroelectric graphene FETs presented in the previous chapter, graphene transferred onto poled-up regions is nearly intrinsic in air, while graphene on poled-down regions is highly p-doped. It is further demonstrated that the resulting junctions can be tuned from p-i- to p-n- junctions through the application of a gate potential. In a last step, the concept of spatial carrier control is demonstrated with graphene on arbitrarily writable domains in $PbZr_{0.2}Ti_{0.8}O_3$ thin films, opening the way to create spatially controllable carrier density modulation in graphene, which is expected to go down to small domain sizes on the nanometer scale.

5.1 Graphene on Periodically Poled $LiNbO_3$

As discussed before, the ferroelectric polarization is expected to stabilize electrons in a graphene film if it is pointing toward the graphene and stabilize holes if the polarization is pointing in the opposite direction. It has been shown that this behavior can indeed be achieved if the polarization is switched with graphene electrodes, but a significant impact of adsorbed molecules has also become apparent. In order to utilize polydomain ferroelectrics for carrier manipulation in graphene, the impact of

the polarization on graphene that is transferred to a polydomain configuration needs to be understood.

This is most easily achieved using commercially available ferroelectrics in which the polarization points in antiparallel directions in different regions of the same sample. A prominent example of such a ferroelectric is periodically poled $LiNbO_3$, which is commonly used for the creation of high power density green or blue laser light through second harmonic generation [75]. The periodic poling with a domain width in the range of 5 to 40 µm is usually achieved through the application of very high electrical fields to unipolar single crystal wafers of $LiNbO_3$ after the definition of a stripe-pattern using photolithography. The photoresist pattern then acts as an insulator preventing ferroelectric switching in the desired areas. The electric field can be applied through an easily removable LiCl electrolyte solution. Utilizing the insights gained from the graphene/$PbZr_{0.2}Ti_{0.8}O_3$ hybrid structures, a comparable impact on the graphene doping level through $LiNbO_3$ is expected, because its high remanent polarization of $\sim$70 µC·cm^{-2} similarly exceeds the available carrier density in a graphene layer.

Due to its high spatial resolution and its nondestructive nature, Raman spectroscopy is the ideal characterization tool to analyze the spatial distribution of carrier densities in graphene films. Secondly, the possibility of characterization of as-prepared samples without the need for device fabrication is desirable because the typical processes involved in device fabrication can potentially screen observed effects or change the nature of the interaction due to photoresist residues and doping from the electrical contacts [31, 76]. Additionally, Raman spectroscopy probes the graphene layer and the underlying crystal structure simultaneously, which allows for the extraction of spatial correlations in the observed doping effects in graphene with the ferroelectric polarization of the $LiNbO_3$.

The domain structure of $LiNbO_3$ can be mapped using polarized Raman spectroscopy because of the interaction of the incoming light with optical phonons in

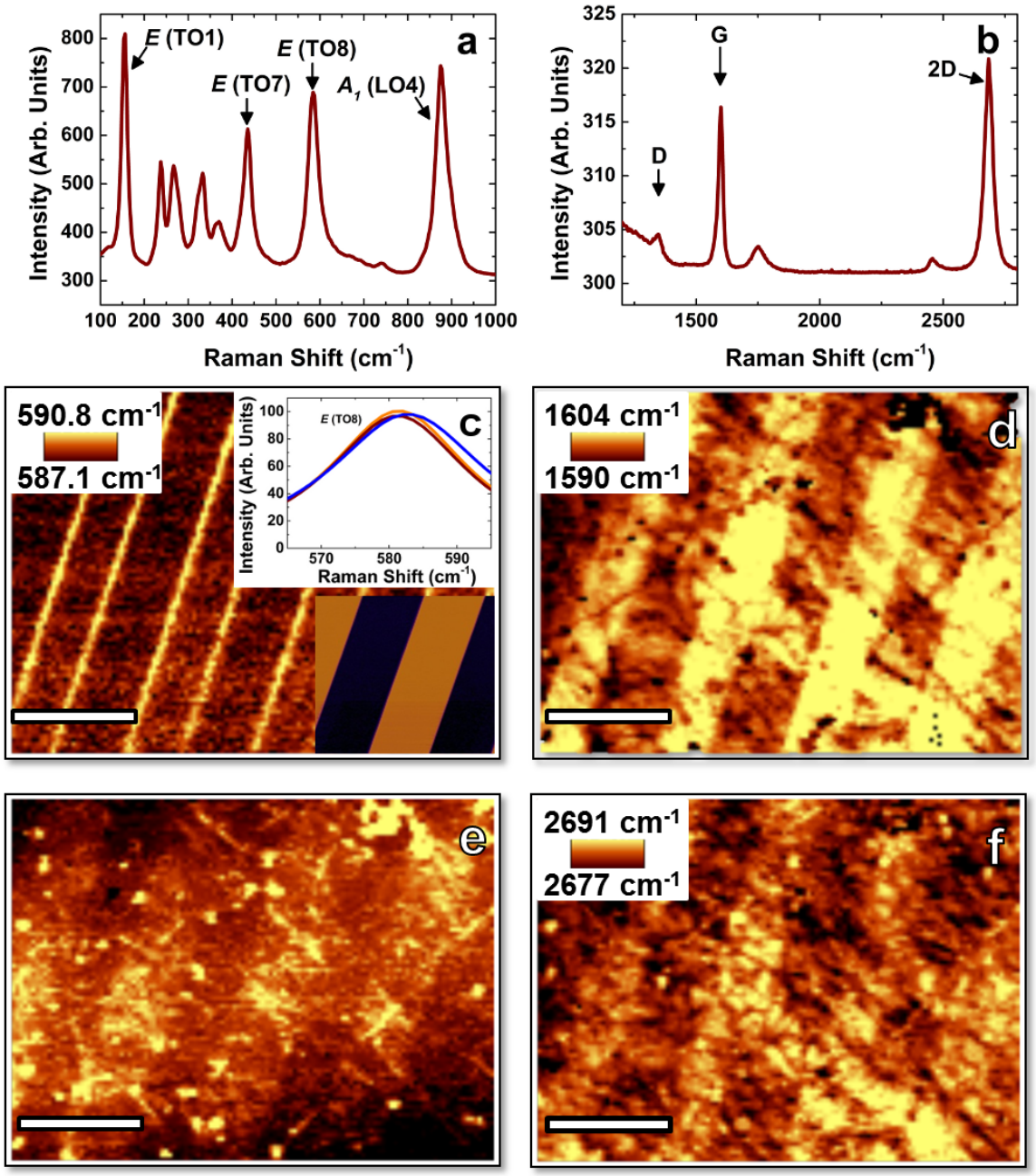

Figure 5.1: Raman characterization of graphene on periodically poled $LiNbO_3$ with 600 mm^{-1} grating. a) Characteristic spectrum of $LiNbO_3$. b) Characteristic average spectrum of graphene on periodically poled $LiNbO_3$. The spectrum is averaged over a 20×20 μm^2 area containing up- and down-polarized domains. c) $LiNbO_3$ E(TO8) frequency map. Upper inset: Lorentzian fits to the E(TO8) peak in up- and down-polarized domains (dark red and orange lines, respectively) as well as for the area in the vicinity of a domain wall (blue line). Lower inset: PFM phase image of the same $LiNbO_3$ sample before graphene transfer. d) Graphene G-band frequency map. e) Graphene 2D-band integrated intensity map. f) Graphene 2D-band frequency map. All scale bars are 8 μm.

the crystal. Their energy and the coupling coefficients depend on the stress fields introduced through the creation of antiparallel domains. These stresses due to the different positions of Nb^{5+} and Li^{+} ions are strongest at the domain wall, but extends far into the domains, which makes them discernible *via* Raman peak position and intensity [77, 78].

The frequency of the so-called E(TO8) band, which corresponds to lattice vibrations along the x- or y-axis of a $LiNbO_3$ crystal can therefore be used to map the domain structure of a periodically poled crystal [figure 5.1a and c]. The frequency significantly blue-shifts at the domain wall and is also different in the bulk of domains pointing up or down. The thin, bright stripes shown in figure 5.1c therefore correspond to the domain walls, the darkest (intermediate) broad stripes map the up (down) polarized domains. A PFM image detected prior to graphene transfer reveals the same 5-µm-periodicity as the Raman map and therefore further confirms the findings of the Raman analysis [figure 5.1c, inset].

Utilizing the broad spectrum of the WITec alpha300 Raman spectrometer, the characteristic graphene peaks can be resolved and mapped simultaneously to the $LiNbO_3$ peaks for the 600 mm^{-1} grating. A map of the graphene G-band frequency for the same area reveals doping regimes which correspond to the different domains in the underlying ferroelectric [figure 5.1d]. The bright stripes corresponding to high carrier concentration in the graphene film occur on the poled-down domains, the dark stripes separating the areas of high doping correspond to significantly lower doping levels (compare section 3.2.3). Very sharp transitions between high and low carrier concentration at the ferroelectric domain walls are apparent. This could be particularly useful for the utilization of ferroelectrically driven carrier modulation in graphene channels for future nanoelectronic devices. As discussed in section 3.2.3, the periodic carrier density in the graphene layer is also expected to result in slightly different 2D-band frequencies and intensities in the respective doping regimes. The

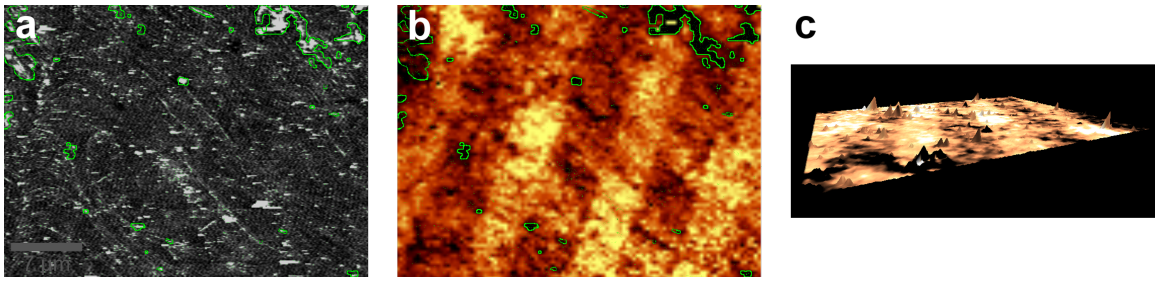

Figure 5.2: Comparison of G-band frequency with the topography. a) AFM topography. b) G-band frequency from figure 5.1d with a green outline corresponding to topographic features. c) 3-dimensional image of the topography in a). The colorscale corresponds to the detected G-band frequency. The dark regions in the G-band frequency clearly corresponds to topographic features.

existence of these stripes in the 2D-band maps detected simultaneously to the $E(\mathrm{TO8})$ map therefore confirm the observed doping phenomenon [figure 5.1e and f].

As is clear from figure 5.1d, the contrast within each dark or bright stripe is not entirely uniform, in fact there appear to be small dark features in different areas of the map. The reason for this non-uniformity becomes directly apparent when the unique capability of combined atomic force microscopy and Raman spectroscopy offered by the WITec alpha300 is used. This allows for the detection of scanning probe topography images along with Raman mapping of the same area. Figure 5.2a shows the topography image for the same area as the maps in figure 5.1. For easier comparison, the graphene G-band frequency map is overlaid with an outline of the topographic features in panel b and in a three-dimensional representation in figure 5.2c. From the overlaid topographic and Raman data it is obvious that the small, dark non-uniformities in the Raman maps correspond to topographic features such as small regions of thicker graphene or transfer residues. Few-layer graphene is known to exhibit smaller dependence of the phonon frequencies on the applied potential, in this case the ferroelectric polarization, and transfer residues can either partially screen the coupling between the graphene and the underlying ferroelectric or lead to a constant, comparably small doping level in their vicinity. Both of these mechanisms can

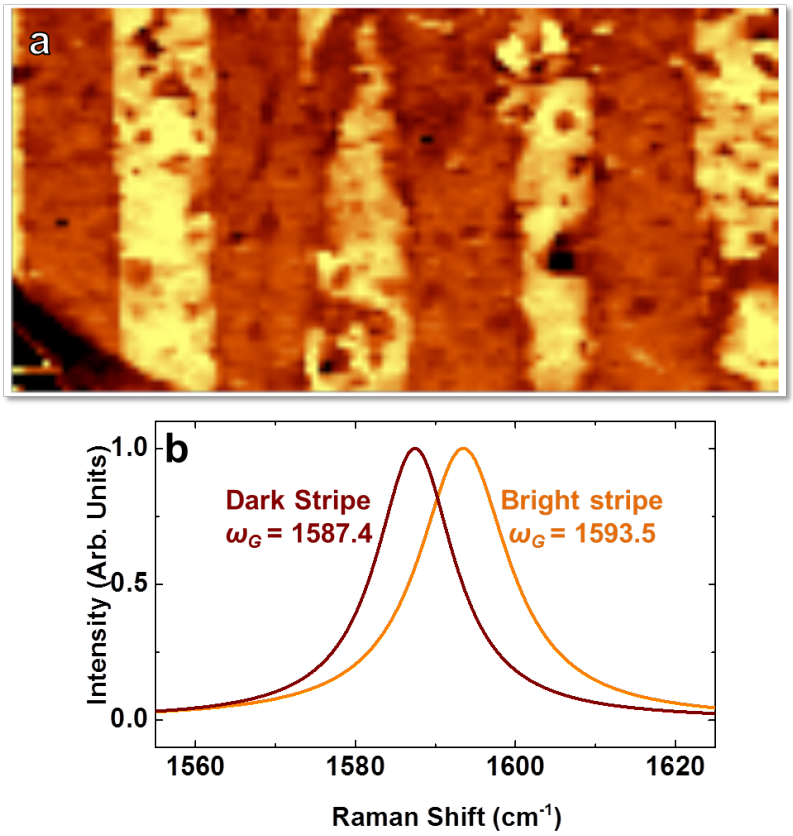

Figure 5.3: Raman signal of graphene on periodically poled $LiNbO_3$ with 1800 mm^{-1} grating. a) Graphene G-band frequency map. b) Normalized graphene G-peak averaged over a dark and a bright stripe in the map in a).

also account for the higher 2D-band integrated intensity corresponding to the dark regions in the G-band frequency [figure 5.1e]

While the observation of a high doping level on down-polarized domains along with a lower carrier concentration on up-polarized domains, which are valid for most of the sample area with the exception of transfer residues or thicker graphene areas, corresponds to the expected behavior, a more detailed analysis of the Raman signal is necessary to extract quantitative information. For this purpose, a similar mapping procedure to figure 5.1d is performed with a higher spectral resolution below 1 cm^{-1} (1800 mm^{-1} grating) [figure 5.3a]. The average peaks for both the dark and bright stripes are fitted to single Lorentzian peaks. The peak position difference (1593 and 1587 cm^{-1} for bright and dark stripes, respectively) is clearly visible in figure 5.3b.

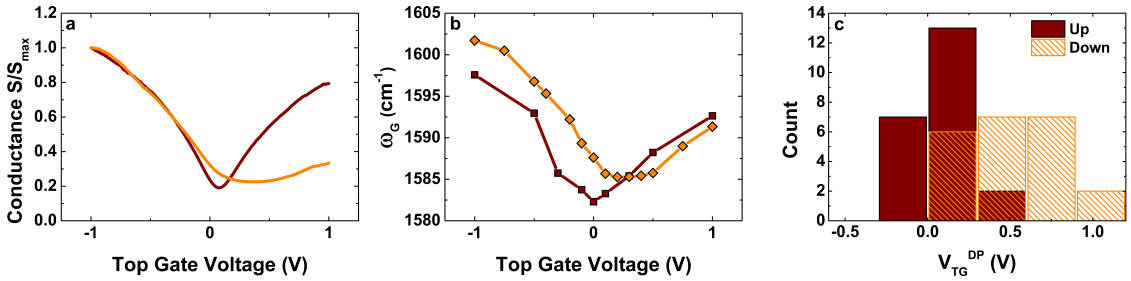

Figure 5.4: Analysis of doping level in top gated graphene devices on unipolar $LiNbO_3$. a) Transfer characteristic of representative top-gated graphene transistors on $LiNbO_3$, which is completely poled-up (dark red) or all poled-down (orange). b) Gate-dependent Raman G-band frequency for the devices shown in a). c) Distribution of the Dirac point voltage V_{TG}^{DP} for graphene devices on unipolar up-polarized (dark red) or unipolar down-polarized $LiNbO_3$ (orange).

This difference in peak position is expected to correspond to a carrier density change of at least 6×10^{12} cm^{-2} if both stripes are p-doped (compare figure 3.10 and ref. [79]), which is remarkably similar to the carrier density change upon polarization reversal in graphene/$PbZr_{0.2}Ti_{0.8}O_3$ hybrid structures (compare Chapter 4).

The doping level in the different stripes can be further understood if a gate potential is applied. As described in section 3.1.4, this can easily be achieved using a PEO electrolyte solution. As a reference, top-gated graphene transistors on unipolar $LiNbO_3$ are fabricated and analyzed [figure 5.4]. The representative transfer characteristics (panel a) and top gate dependent Raman G-band shift (panel b) on a down-polarized sample reveal heavily p-doped behavior, while the device on a down-polarized sample is nearly intrinsic, which is expected as the electrolyte solution can isolate the graphene from the p-doping air environment. The representative characteristics shown here fall well into the distribution for multiple devices on the same sample (panel c). Using the same top-gating procedure on a periodically poled sample, the gate dependent Raman shift of both the bright and the dark stripes can be used to gain further insight in the actual doping level and carrier type of the graphene [figure 5.5]. The same trend as observed for graphene/$PbZr_{0.2}Ti_{0.8}O_3$ hybrid structures and devices on unipolar $LiNbO_3$ is observed for the corresponding stripes, i.e.

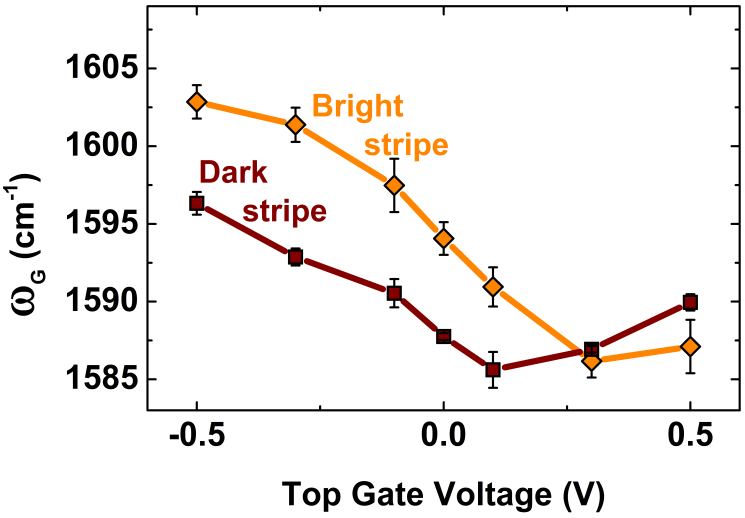

Figure 5.5: Analysis of doping level in each stripe. Gate-dependent average Raman G-band frequency for dark and bright stripes (dark red squares and orange diamonds, respectively) for a transistor showing similar features as presented in figure 5.1 and figure 5.3.

graphene is p-type on poled-down domains and slightly p-type or intrinsic on poled-up areas. The actual carrier density can be calculated utilizing the gate capacitance per unit area C_{PEO} according to

$$n = C_{PEO}\frac{V_G}{e} \tag{5.1}$$

with the applied gate voltage V_G, $C_{PEO} = \frac{\epsilon\epsilon_0}{\lambda}$, the Debey length $\lambda = \sqrt{\frac{\epsilon\epsilon_0 kT}{2\rho e^2}}$, the electrolyte concentration ρ, the unit charge e, the dielectric constant of the PEO $\epsilon \sim$10 and the thermal energy kT [56]. With the salt concentration $\rho = 2.4$ mol·L^{-1} and the resulting capacitance $C_{PEO} \sim 4$ μF·cm^{-2}, equation 5.1 yields a carrier density difference of 5-6×10^{12}, further validating the observed Raman frequencies.

In addition to the creation of spatial carrier modulation, figure 5.5 clearly demonstrates that the application of top gates allows for p-n-junctions to be created in graphene on periodically poled $LiNbO_3$ if the gate voltage is chosen between the Dirac points for both stripes. For this particular device a voltage between 0.1 and

0.3 V induces n-type behavior in regions on up-polarized $LiNbO_3$, while the graphene on down-polarized $LiNbO_3$ is still p-type. This means that through the application of a gate voltage to the entire channel area a p-n-junction can be turned on or off. This yields distinct advantages over previously reported p-n-junctions in graphene through the application of split gates, which are limited by lithographically available size, introduce complicated fabrication and require multiple electrical connections to a single device [80–83].

A more complete characterization of p-n-junctions in graphene can be obtained *via* scanning photocurrent microscopy. In this setup, a laser with a small spot size is scanned across a graphene device with grounded electrodes. The induced photocurrent is measured at one of these contacts. At local potential steps within the graphene, the internal electric field causes the excited carriers to be separated and accelerated into opposite directions. Assisted through other mechanisms, such as thermal electric currents [84] and hot-carrier assisted non-local transport [85], a sensitivity of up to 1 mA/W has been achieved with exfoliated graphene devices. These thermal effects are caused by local heating due to the laser energy input. Locally, the electrons posses a higher temperature than the bulk of the sample, leading to a thermal current away from the local hot spot. In a homogeneously doped graphene sample away from the metal contacts, this leads to an isotropic current resulting in a zero net-current at the contacts. If the graphene sheet exhibits local potential steps, the carrier density and type dependent Seebeck coefficient S leads to a photoresponse that can be detected at the contacts according to

$$V_T = (S_1 - S_2)\,\Delta T \tag{5.2}$$

with the thermovoltage V_T, the Seebeck coefficients S_1 and S_2 and the temperature gradient ΔT. This results in a detectable photocurrent at each potential step within

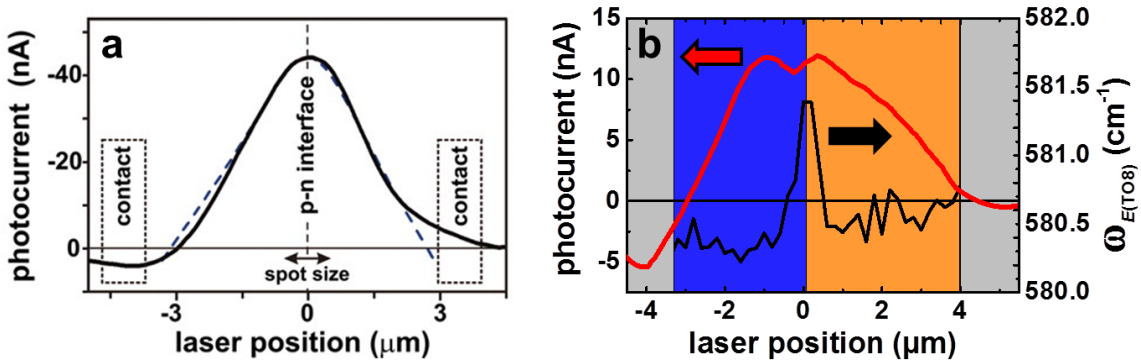

Figure 5.6: Graphene photocurrent response. a) Photocurrent detected in a graphene p-n-junction created through global back-gates and local top-gates. Reprinted with permission from [85]. b) Photocurrent response of a top-gated graphene transistor with a gate voltage of 400 mV on periodically poled $LiNbO_3$ and Raman E(TO8) frequency along the same line. The Raman signal can be used to identify the down-polarized (orange) and up-polarized (blue) domains of the $LiNbO_3$. Grey shading corresponds to the Ti/Pd contacts. For each data point, the current was integrated for 10 seconds and then averaged over neighboring points.

the graphene film. These can either be carrier density steps within the channel or close to the contacts. These steps exist in typical graphene transistors due to the constant slight p-doping observed in the vicinity of Pd or Ti/Pd electrodes. Depending on the majority carrier density, these steps can lead to a negative or positive photocurrent response.

The typical photocurrent response of a graphene p-n-junction is depicted in figure 5.6a. Comparably small currents at the contacts and a strong response within the graphene channel are detected for this particular device because the laser wavelength is chosen such that the electrodes experience a minimum heating effect and because the carrier density is tuned in a way that reduces the size of the potential steps near the contacts while maximizing the potential step at the p-n-interface. The remarkable capability of graphene/ferroelectric hybrid structures to create p-n-junctions at the ferroelectric domain walls through the application of a single gate potential becomes apparent when comparing the photocurrent response in top-gated graphene devices on periodically poled $LiNbO_3$ with the well-characterized response in p-n-junctions

achieved through split gates [figure 5.6b]. Using a scanning photocurrent measurement setup combining the stage scanning capabilities from the Jobin Yvon Labram HR800 micro-Raman with electrical probes connected to the Agilent Semiconductor Parameter Analyzer 4155C, the photocurrent response can be spatially resolved down to the laser spot size of ∼1 µm. With a gate voltage of 400 mV and laser excitation with 532 nm and ∼700 µW, a photocurrent response that is maximized near the independently determined domain wall position is detected. Local kinks in the curve stem from limited spatial resolution due to stage movement capabilities and potentially local potential variations caused by photoresist residue. Photolithographically defined electrodes were chosen in this case to ensure alignment of the graphene channel with only one domain wall in the channel, which is not accessible with shadow masks. The qualitative agreement of the photocurrent response of the graphene/$LiNbO_3$ hybrid structure with the expected result strongly highlights the desirable effects which can be created in graphene on polydomain ferroelectrics.

The quantitative information from figure 5.6b can be compared to the extracted carrier densities from the Raman analysis. A potential step of approximately 0.2 eV has been shown to lead to a maximum photocurrent response of 0.3 mA/W for exfoliated graphene on SiO_2 [86], which typically exhibits much higher carrier mobilities than the graphene/ferroelectric devices used here. Using the relationship

$$\Delta E = \hbar v_F \sqrt{n} \tag{5.3}$$

with the potential step between the p- and n-doped regions ΔE, the Planck constant $\hbar$ and the Fermi velocity v_F [76], a carrier density step of 6×10^{12} cm^{-2} corresponds to a potential offset of 0.13 eV. The comparably low responsivity of 0.02 mA/W for the device shown in figure 5.6b can be explained through the order of magnitude difference in mobility. Chemical vapor deposition grown graphene has been demonstrated to

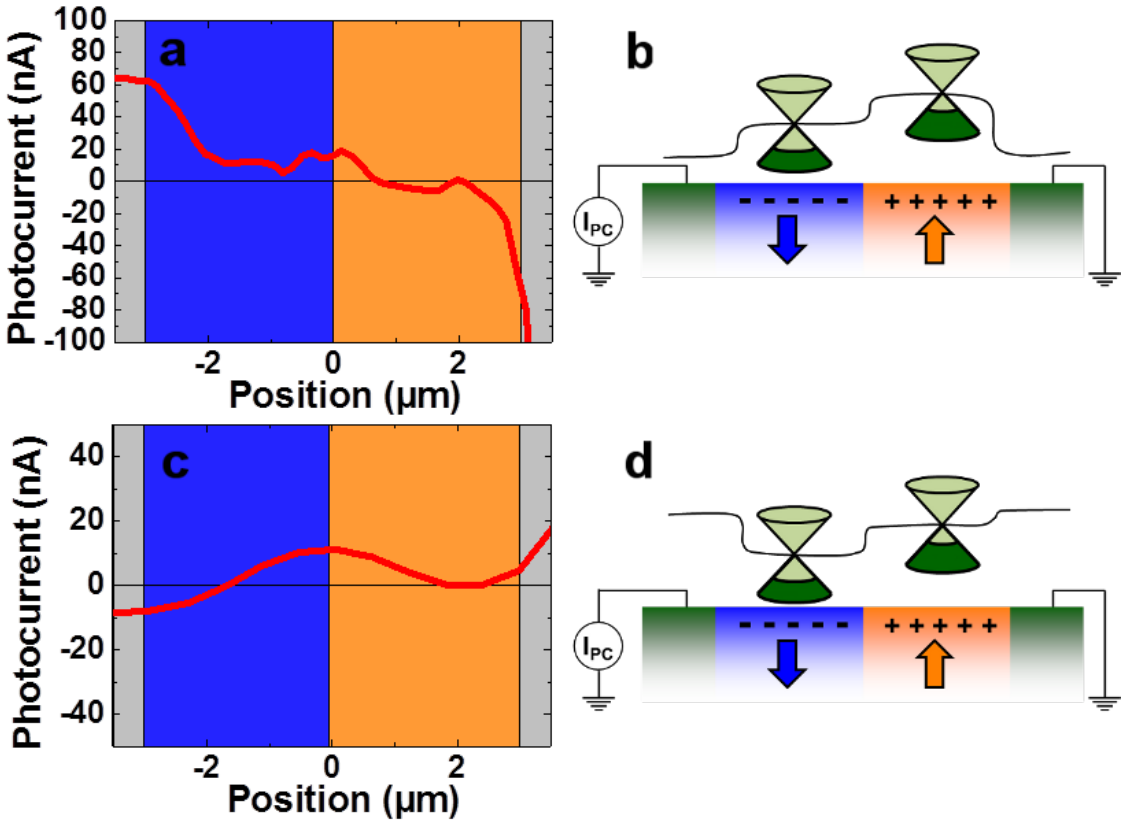

Figure 5.7: Graphene photocurrent response for different global gate potentials. a) Photocurrent response of a top-gated graphene transistor on periodically poled $LiNbO_3$ without an applied gate potential. b) Schematic band diagram of the p^+-p-junction for the device in a. c) Photocurrent response of the same device with a gate voltage of 400 mV. d) Schematic band diagram of the n-n^+-junction for the device in c. The Raman E(TO8) frequency was used to identify the down-polarized (orange) and up-polarized (blue) domains of the $LiNbO_3$. Grey shading corresponds to the Ti/Pd contacts. For each data point, the current was integrated for 10 seconds and then averaged over neighboring points.

possess a reponsivity of 0.05 mA/W for a device with about 2-3 times the mobility of the graphene/ferroelectric hybrid devices [87]. The measured photocurrent therefore exhibits the expected order of magnitude.

The possibility to tune the potential steps in graphene devices on polydomain ferroelectrics from p^+-p to p-n to n-n^+-junctions through the application of a single gate for the entire channel area is depicted in figure 5.7. In this device, the photocurrent response without an applied gate voltage clearly indicates that a p^+-p-junction exists at the domain wall, which gives rise to very strong photocurrent not only in the vicinity of the junction, but also close to the contacts [figure 5.7a and b]. Through the application of a global gate voltage, this junction can be transformed to a n-n^+-junction [figure 5.7c and d]. This leads to a reversal of the sign of the photocurrent response at both contact edges, while the photocurrent at the domain wall remains constant because this potential step is not reversed but shifted from the p-doping regime to the n-doping regime. The ratio of the photocurrent magnitude at the ferroelectricity-induced potential step and at the edges is expected from the schematic band diagrams in figure 5.7b and d and is discussed in more detail in section 5.2.

5.2 Graphene on Dual-domain $PbZr_{0.2}Ti_{0.8}O_3$

The availability of local carrier density modulations and tunable p-n-junctions in graphene on polydomain ferroelectrics can also be extended to thin film ferroelectrics, which allow for the creation of artificial domain structures down to the nanoscale. The combination of nanoscale domains with the local carrier concentration control is highly desirable for the carrier manipulation in future nanoelectronic devices. Here, the well-characterized graphene/$PbZr_{0.2}Ti_{0.8}O_3$ hybrid structures are modified to demonstrate this exciting possibility. As demonstrated in Chapter 4 and figure 5.8, graphene on up- and down-polarized $PbZr_{0.2}Ti_{0.8}O_3$ in air is expected to exhibit

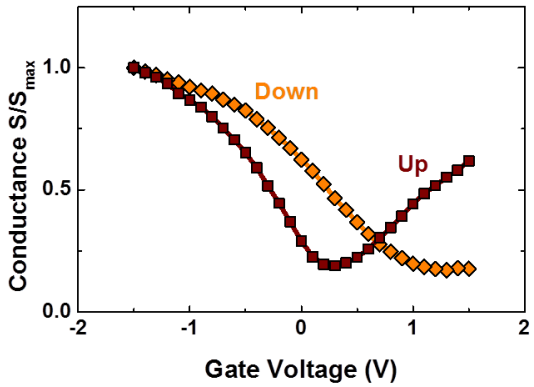

Figure 5.8: Transfer characteristics for a graphene/$PbZr_{0.2}Ti_{0.8}O_3$ hybrid device in air. The orange diamonds and dark red squares correspond to the $PbZr_{0.2}Ti_{0.8}O_3$ being poled up or down, respectively. The polarization was switched using a 1 ms 5 V gate voltage pulse.

slightly p-doped and highly p-doped behavior, respectively. With the application of a gate voltage or environmental control, the junction between the different domains is expected to be tunable to a p-n-junction.

The modified device fabrication is schematically demonstrated in figure 5.9. Prior to graphene transfer, the desired domain configuration in a $PbZr_{0.2}Ti_{0.8}O_3$ film was defined using PFM. The SiO_2/Ti/Pd contact pads were used as alignment markers. In a last step, Pd top electrodes were deposited and the channel was isolated using oxygen plasma. The domain configuration was shown to slightly relax under oxygen plasma with the conditions used here [figure 5.10]. A protective layer of graphene and photoresist is anticipated to ensure that the desired domain configuration was still present underneath the graphene channel at the end of the fabrication process. Slight deviations from sharp junctions in the resulting graphene devices, however, might be caused through partial relaxation of the domain configuration.

To demonstrate the ability to create p-n-junctions within a graphene channel using thin film ferroelectrics, devices similar to the graphene/$LiNbO_3$ device shown in figure 5.6b were compared with control devices with a monodomain $PbZr_{0.2}Ti_{0.8}O_3$ film underneath the graphene channel [figure 5.11a]. The emulation was achieved by

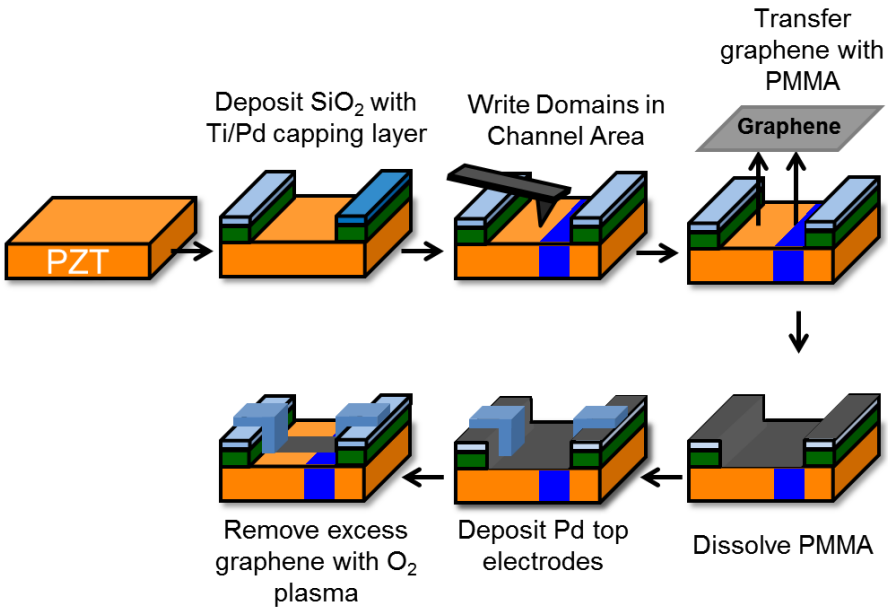

Figure 5.9: Fabrication of graphene transistors on polydomain $PbZr_{0.2}Ti_{0.8}O_3$ using the one-touch transfer described in section 3.1.4. Prior to graphene transfer, PFM is used to define the desired domain configuration between the SiO_2/Ti/Pd contact pads. Photolithography, electron beam evaporation and oxygen plasma treatment lead to the desired device designs.

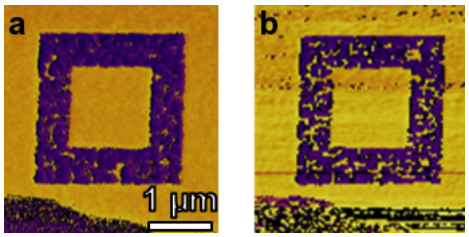

Figure 5.10: Domain stability under oxygen plasma treatment. a) PFM phase image of a written domain. In the bottom left corner of the scan, an alignment marker is visible. b) PFM phase image of the same domain after oxygen plasma treatment with 50 W for 20 s.

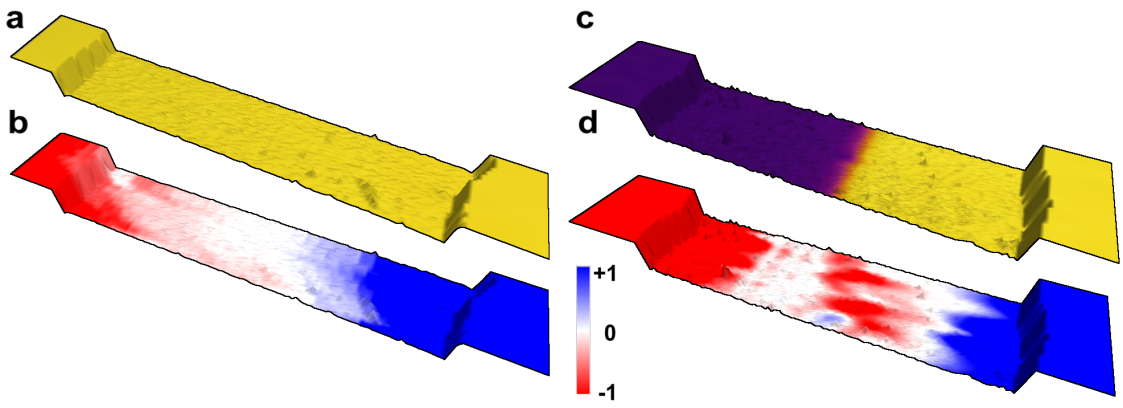

Figure 5.11: Photocurrent response of graphene/$PbZr_{0.2}Ti_{0.8}O_3$ hybrid devices with different domain configurations. a) PFM phase image overlaid with the topography data for a device with a monodomain channel. b) Normalized photocurrent response for the device in a. c) PFM phase image overlaid with the topography data for a device exhibiting up-polarized $PbZr_{0.2}Ti_{0.8}O_3$ (yellow) for approximately half the channel and down-polarized $PbZr_{0.2}Ti_{0.8}O_3$ (violet) for the other half. d) Normalized photocurrent response for the device in c).

creating a single domain of down-poled $PbZr_{0.2}Ti_{0.8}O_3$ in an otherwise up-polarized film for approximately half the channel area, resulting in a "dual-domain" channel [figure 5.11c]. Photocurrent measurements without an applied gate potential reveal the expected response at the electrode edges. For the monodomain channel, a monotonous transition from a positive current at one edge to an equal and opposite current at the second electrode is observed [figure 5.11b]. This behavior is expected from a rather homogeneously p-doped graphene channel [76, 84, 88]. The observed characteristic for the device with a dualdomain channel, however, is distinctly different. Instead of a smooth transition, a negative current is observed close to the domain wall over the entire map [figure 5.11d] and in each individual line [figure 5.12a]. For the line scan for the polydomain sample, the difference in magnitude for the different contacts is also to be expected because of the potential steps in the vicinity of the contacts is not equal.

In fact, the photocurrent can be explained well by the potential variations in graphene as schematically shown in figure 5.11d [figure 5.12b]. Close to the contacts,

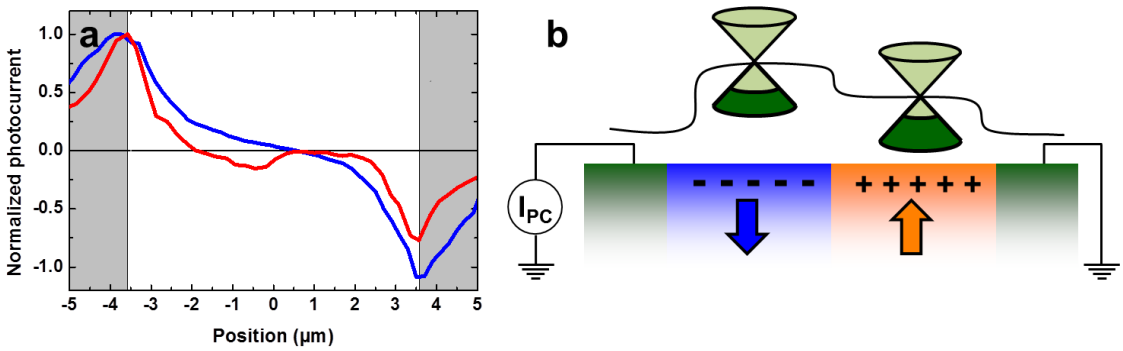

Figure 5.12: Analysis of the photocurrent response in graphene/$PbZr_{0.2}Ti_{0.8}O_3$ hybrid devices. a) Representative photocurrent response along a horizontal line for the device shown in figure 5.11a and b (blue line) and for the device shown in figure 5.11c and d (red line). b) Schematic band diagram for the device in figure 5.11d.

the device is expected to be nearly intrinsic but slightly p-doped. In the bulk of the channel, the graphene exhibits a higher p-doping level on the up-polarized domain and the highest hole concentration in the area covering the down-polarized domain. The resulting photocurrent can be entirely explained with the features presented in figure 5.12b. When collecting the photocurrent at the contact close to the down-polarized domain, strong negative current is detected when the laser light illuminates the vicinity of that contact because of the large positive potential step. Similarly, negative current of slightly smaller magnitude is expected at the second electrode. At the domain wall, a negative current is created because electrons are accelerated away from the contact used for current collection. The smaller magnitude indicates that the junction at the domain wall exhibits a smaller potential step than the junction close to the contact. This is expected without an applied gate voltage in air.

The results presented in this chapter clearly demonstrate that even though charged species opposing the ferroelectric polarization are expected to be present on ferroelectric surfaces prior to graphene transfer, the coupling of the graphene doping

level to the ferroelectric polarization is strong enough to create ferroelectrically driven carrier density modulations, which are comparable in magnitude to the results obtained with split-gate induced p-n-junctions. This opens the possibility to create potential steps in graphene devices that can be tuned from p^+-p to p-n to n-n^+ junctions through the application of a single gate for the entire channel area. Domain engineering down to the nanoscale opens the way to utilize graphene as a channel material with multiple p-n-junctions for future nanoelectronic devices, which might then yield desirable effects such as high on-off ratios in transistor-like devices while maintaining the unparalleled mobilities accessible in graphene [6].

Chapter 6

Conclusion and Outlook

The combination of two important classes of functional materials with exciting prospects for future nanoelectronic applications (i.e. carbon nanoelectronics and complex oxide thin-film electronics) may lead to a range of new phenomena being accessible for observation, scientific characterization and understanding, as well as for application in future electronic devices. In this thesis, significant advancement in the integration of two prominent representatives of these material classes - graphene and ferroelectric oxides - has been achieved through a combination of advanced fabrication, device operation and characterization. These steps result in the direct control of the carrier density in graphene through the ferroelectric polarization in FET devices and spatially periodic geometries.

To date, the operation of devices based on graphene integrated onto ferroelectric oxides has primarily been dominated by extrinsic effects arising from adsorbed molecules, as was summarized in Chapter 2. The graphene/$PbZr_{0.2}Ti_{0.8}O_3$ hybrid-structures fabricated and characterized as discussed in Chapter 3, however, have been proven to exhibit bidirectional interdependency between the graphene doping level and the ferroelectric polarization. As discussed in Chapter 4, the polarization of the $PbZr_{0.2}Ti_{0.8}O_3$ can be switched using graphene-based electrodes, enabling reliable and fast operation with low voltages, which in turn can change the doping level in graphene channels. One of the most striking consequences of ferroelectric polarization switching dominating electron transport in graphene is the complete reversal of the hysteresis direction in transistor devices. This reversible and permanent switching

behavior can now be used in non-volatile ferroelectric graphene transistors. The generality of the results obtained here is verified through the implementation of graphene with ferroelectric $BiFeO_3$ in Appendix A.

The on/off ratio of these devices, however, is limited due to the zero-gap nature like any graphene transistor. Therefore, the utilization of polydomain ferroelectrics for complex carrier manipulation in graphene has been explored in Chapter 5. In particular, the possibility of collective excitations in periodic carrier density configurations and the exploitation of chiral tunneling of massless Dirac fermions in graphene p-n-junctions may lead to new ways to utilize carrier manipulation in graphene channels for future nanoelectronic devices such as switches or memory devices.

Through the detailed characterization with Raman spectroscopy and scanning photocurrent measurements, the creation of potential steps in graphene at domain walls of the underlying ferroelectric has been demonstrated. Carrier density modulations of approximately 5×10^{12} cm^{-2} now provide a platform that offers graphene devices exhibiting potential steps which can be tuned from p^+-p to p-n to n-n^+ junctions through the application of a single gate for the entire channel area. This is particularly useful for the implementation and utilization of the exciting two-dimensional phenomena in graphene.

Therefore, the future work in the implementation of graphene with complex oxides should focus on the carrier manipulation in graphene devices exhibiting multiple p-n-junctions created through the underlying ferroelectric domain structure. The creation of multiple junctions at different angles in the same graphene channel has been predicted to open a transport gap in graphene, while the high carrier mobility remains intact. The suggested utilization of the results demonstrated in this thesis for future graphene electronics based on chiral tunneling across p-n-junctions is briefly summarized in Appendix B. The accessibility of deterministically tunable domain structures in ferroelectric films down to the nanoscale provides a significant advantage

over existing technologies such as split gates. Additionally, the availability to tune the junctions from p^+-p to p-n with a single gate makes the implementation of such devices much easier.

One of the major difficulties in the implementation of such devices may be the necessity of ballistic transport throughout multiple junctions, which is most easily achieved with short channel areas and high mobilities. Therefore, the alignment of ferroelectric domains with the electrodes should be performed using electron beam lithography rather than conventional photolithography. Moreover, measurements at cryogenic temperatures may enable the observation of effects otherwise screened through enhanced scattering at room temperature. The same might be achieved with a thin layer of hexagonal boron nitride between the graphene and the ferroelectric surface. The introduction of such an insulating layer is expected to increase the graphene mobility, but additional screening of the polarization could complicate the coupling to the graphene carrier density.

Additionally, the difficulties associated with adsorbed molecules on the ferroelectric surface prior to graphene transport and the existence of local polymer residues introduced during the transfer process can impair the control of the doping level through the polarization and the sharpness of the created p-n-junctions. Therefore it would be highly desirable if graphene could be grown directly on the ferroelectric surface. This might significantly enhance the potential steps accessible in the hybrid devices, because a complete compensation of the ferroelectric polarization through the graphene would correspond to unparalleled carrier densities. The direct growth of single-layer graphene on oxide surfaces, however, has so far been challenging, although recent developments suggest it might be achievable by employing Ni catalysts [89–91].

Taking the integration of oxide and carbon nanoelectronics even further, the implementation of nano-scale electrodes such as nanowires or carbon nanotubes with graphene and ferroelectrics may yield novel and particularly useful characteristics.

In a potential device structure, carbon nanotubes sandwiched between a graphene channel and a ferroelectric film could be used as nano-switches for the ferroelectric polarization, which would allow for non-volatile *in-situ* creation or termination of p-n-junctions at an extremely local scale.

Appendix A

Graphene/$BiFeO_3$ Hybrid Structures

Graphene/ferroelectric hybrid devices can be fabricated with different ferroelectric thin films similar to Chapter 3. To demonstrate this ability, graphene was transferred to $BiFeO_3$ thin films and transistor devices were fabricated.

For this purpose, 180 nm $BiFeO_3$ $(001)_c$/60 nm $SrRuO_3$/$DyScO_3$ (110) heterostructures were fabricated with a two-step *in situ* pulsed laser deposition process employing a KrF excimer laser (wavelength $\lambda = 248\,\mathrm{nm}$) at temperatures of 640 and 730 °C, laser repetition rates of 14 and 10 Hz, and laser fluences of 0.66 and 0.60 J cm^{-2} in oxygen atmospheres of 100 mTorr, respectively. After growth, the films were cooled to room temperature at an oxygen pressure of 760 Torr.

X-ray diffraction of these heterostructures reveals the crystalline quality, absence of second phases and smoothness of the interface and surface [figure A.1]. The Kiessig fringes detectable due to the smoothness have been used to calculate the film thickness. Tapping mode scanning probe microscopy reveals that the roughness of the surface is on the order of 300 pm, an extremely small number for such a thick film [figure A.2a]. Indeed, layers of unit cell thickness can clearly be seen.

The domain structure of the $BiFeO_3$ is slightly more complicated than in the case of $PbZr_{0.2}Ti_{0.8}O_3$ thin films, because the polarization in $BiFeO_3$ points along the pseudo-cubic (111) direction. This means that a significant portion of the polarization is in-plane oriented. On $DyScO_3$ (110) substrates, this leads to a domain formation with long domains of alternating in-plane polarization. These domains form parallel to the sample edges. The out-of plane orientation is down-polarized for the entire film

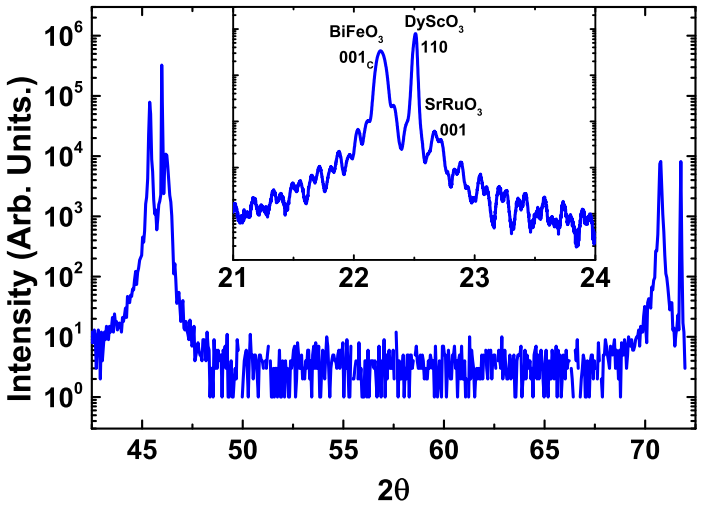

Figure A.1: $\theta - 2\theta$ X-ray diffraction pattern about the pseudo-cubic 001-, 002- and 003-diffraction peaks for the $BiFeO_3/SrRuO_3/DyScO_3$ thin film heterostructure reveals single-phase, epitaxial film and bottom electrode.

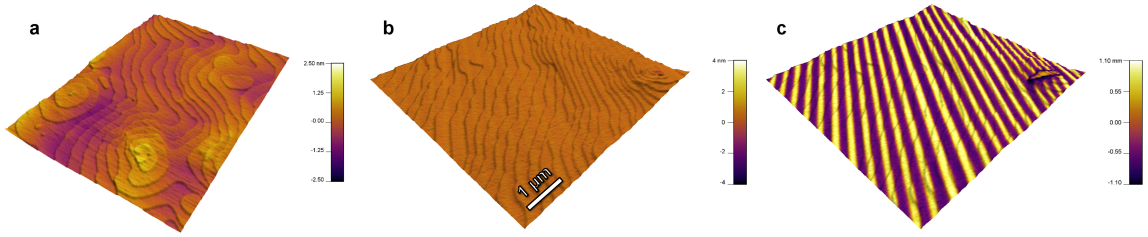

Figure A.2: Scanning probe characterization of $BiFeO_3$ thin films with only two variants of in-plane orientation. a) Tapping mode topography image. b) Out-of-plane PFM amplitude and c) in-plane PFM amplitude in a different region of the same sample overlaid with the topography data.

in the as-grown state. This domain configuration is clearly visible in the out-of-plane and in-plane PFM amplitude images [figure A.2b and c, respectively]. Depending on substrate quality of miscut, only two or four different variants of the in-plane orientation coexist in the $BiFeO_3$ film [figure A.2].

Graphene transistors on $BiFeO_3$ might differ from graphene/$PbZr_{0.2}Ti_{0.8}O_3$ hybrid devices because of the significant amount of in-plane polarization and the existence of antiferromagnetism in $BiFeO_3$, which might couple differently to the carriers in a graphene film. In a first approach, however, the transport characteristics of a

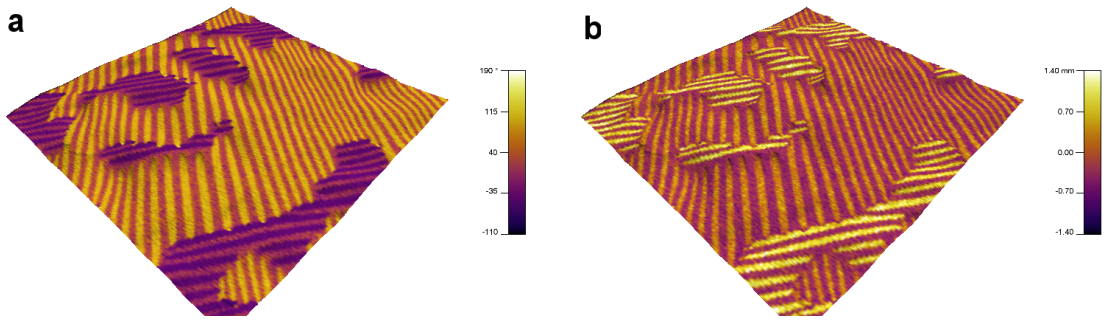

Figure A.3: Scanning probe characterization of $BiFeO_3$ thin films with four variants of in-plane orientation. a) In-plane PFM amplitude and b) in-plane PFM phase image overlaid with the topography data.

graphene transistor on $BiFeO_3$ resemble the characteristics discussed in Chapter 4 [figure A.4]. For slow sweep rates, a non-monotonic point in the drain current accompanied with a rise in the gate current at $V_G = 2.5$ V and a corresponding positive shift of the Dirac point are observed. This corresponds to the case of extrinsic charging effects dominating the hysteresis. As for the graphene/$PbZr_{0.2}Ti_{0.8}O_3$ hybrid devices, fast sweep rates lead to a reversal of the hysteresis direction, making a Dirac point shift to more negative values upon the application of positive gate voltages possible.

A qualitative difference as compared to devices on $PbZr_{0.2}Ti_{0.8}O_3$ lies in the strong reduction of current for positive gate voltages. A similar asymmetry is also present in the devices analyzed in Chapter 4, but the extend is much more pronounced for graphene/$BiFeO_3$ transistors. The reason for this asymmetry, however, is beyond the scope of this thesis. It might be induced by contact problems for this particular sample impeding electron transport in these transistors, or it could hint at a qualitatively different coupling between graphene and $BiFeO_3$.

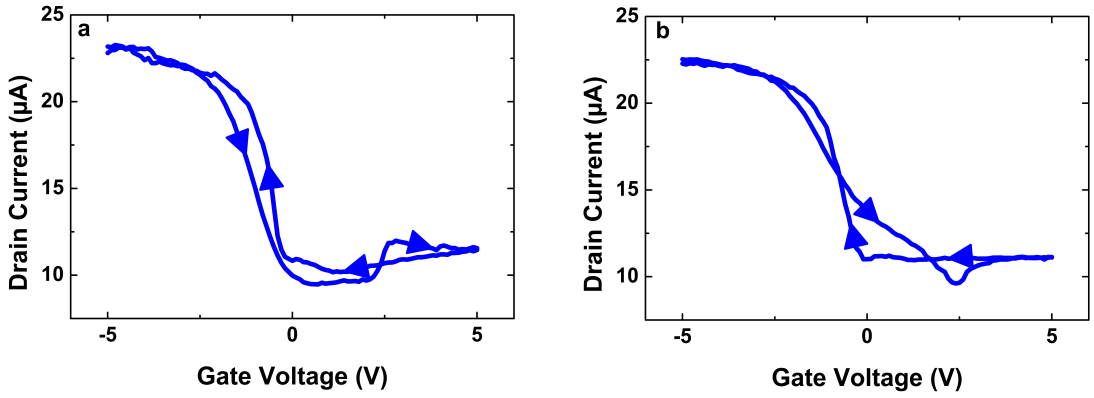

Figure A.4: Transport characteristics of a graphene transistor on $BiFeO_3$. a) Very slow sweep rate, resulting in the well-known feature of a non-monotonic point in the drain current accompanied with a rise in gate current at $V_G = 2.5$ V and a corresponding positive shift of the Dirac point. b) Fast sweep rate. The hysteresis direction is reversed, i.e. the Dirac point shifts to more negative values upon the application of positive gate voltages.

Appendix B

Utilization of Chiral Tunneling in Graphene on Polydomain Ferroelectrics

Using the theoretical predictions by Katsnelson *et al.* [6] and Sajjad *et al.* [10], a gedanken experiment has been suggested which allows for the opening of a transport gap in single layer graphene transistors but is difficult to implement practically with traditional gate dielectrics. Using multiple p-n-junctions within a channel which is shorter than the mean free path of electrons and holes in graphene, the chiral tunneling described in section 2.1 can lead to very small transmission probabilities for certain geometries. If electrons traveling through the channel first have to tunnel through a p-n-junction that is parallel to the source and drain electrodes, the highest transmission probability is observed for electrons traveling normal to this junction [43]. After this junction the majority of remaining electrons will therefore travel in the normal direction. In the absence of defect or edge scattering, the electrons will be traveling in the same direction when they reach the next, slanted junction. As equation 2.3 demonstrates, these electrons will then have vanishing tunneling probability for the second junction, if the angle and barrier height are chosen correctly.

This phenomenon is complicated to utilize with common split gates which are usually used to create p-n-junctions in graphene. The ability to create p-n-junctions at ferroelectric domain walls, however, may significantly improve the accessibility of local p-n-junctions that could be used for such an experiment. In the device shown in figure B.1, p-n-junctions with different angles are expected to arise at the domain walls for certain global gate voltages. Using appropriate alignment and lithography procedures, the channel can be tuned down to the sub-micron scale and the domains

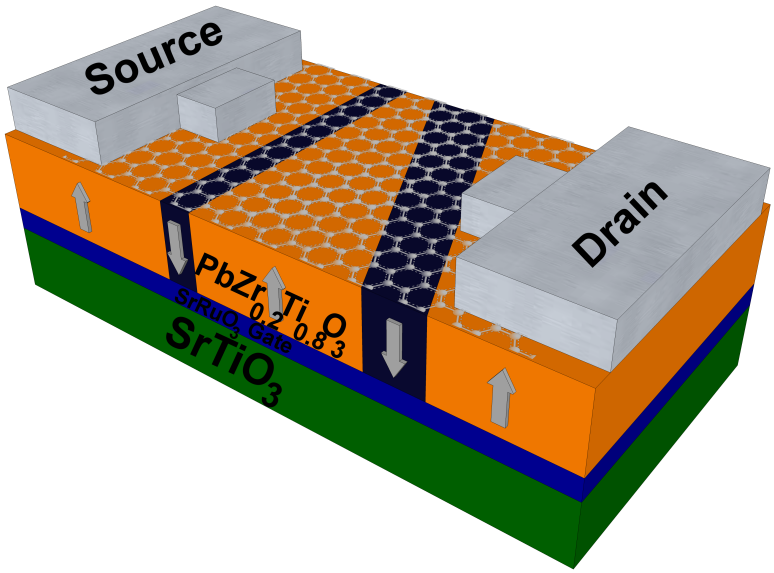

Figure B.1: Suggested device geometry for the utilization of chiral tunneling in graphene/$PbZr_{0.2}Ti_{0.8}O_3$ hybrid devices.

can easily be written at the same scale. Because of the high mobility in graphene, ballistic transport across the entire channel length might be accessible. Due to the comparably low mobility observed so far in graphene/$PbZr_{0.2}Ti_{0.8}O_3$, this might be challenging to achieve. Ballistic transport across multiple domain walls, on the other hand, can be easily achieved if enough care is taken in the alignment of the domain structure within the channel.

The expected device characteristic for such a device is shown in figure B.2. For negative gate voltages, holes are the majority carriers throughout the entire channel, leading to a device performance similar to a classical graphene transistor. When the Dirac point gate voltage for the up-polarized areas is reached with low, positive gate voltages, however, the device characteristic is expected to change dramatically. In the absence of impurity or edge scattering, the current is expected to drop significantly below the observed values for a regular transistor. This transport gap should be achieved for any gate voltage between the Dirac point voltages on the different domains.

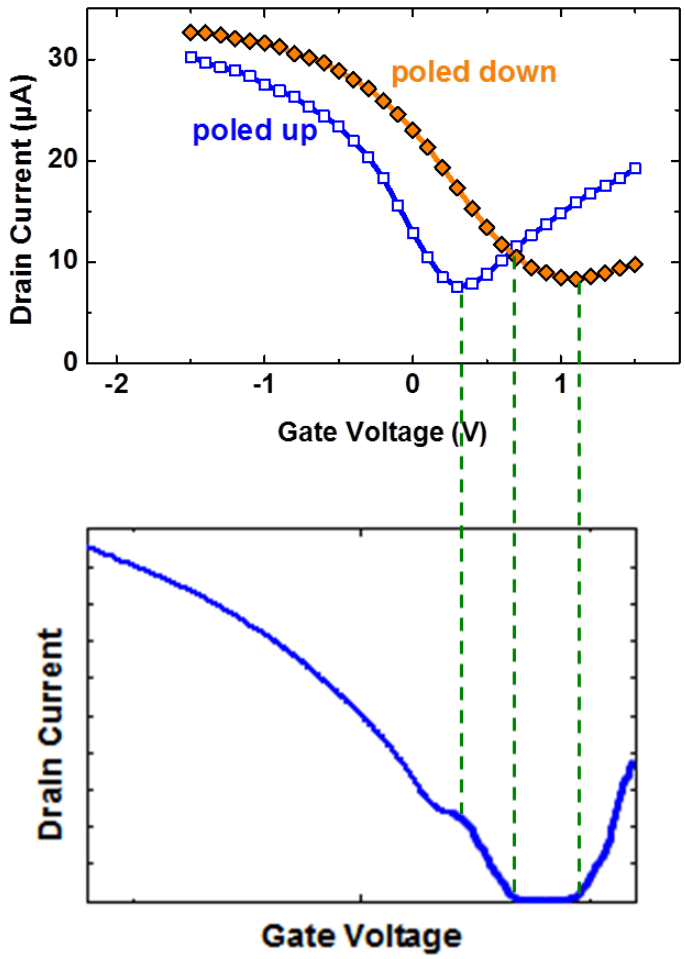

Figure B.2: Expected transfer characteristic for the device shown in figure B.1 assuming ballistic transport and vanishing transmission probability for electrons traveling normal to the electrode edges at the slanted junction. The known transfer characteristics on unipolar $PbZr_{0.2}Ti_{0.8}O_3$ can be used to predict the opening of a transport gap for the gate voltage regime which results in p-n-junctions at each domain wall.

The higher on/off ratio expected from such a device degrades with lower mobilities and in general with increased scattering. Therefore, a complete theoretical and phenomenological investigation for the device geometry and operation needs to be performed to achieve desirable results. Important factors are anticipated to be the channel width and length, the number of domain walls as well as the angle between individual boundaries. This evaluation is beyond the scope of this thesis, but the results from Chapter 5 provide the foundation for such an analysis among other potential applications of graphene/ferroelectric hybrid structures.

References

[1] Novoselov, K. S., Geim, A. K., Morozov, S. V., Jiang, D., Zhang, Y., Dubonos, S. V., Grigorieva, I. V., and Firsov, A. A. *Science* **306**, 666–9 (2004).

[2] Geim, A. K. and Novoselov, K. S. *Nat. Mater.* **6**, 183–91 (2007).

[3] Castro Neto, A. H., Peres, N. M. R., Novoselov, K. S., and Geim, a. K. *Rev. Mod. Phys.* **81**, 109–162 (2009).

[4] Zhang, Y., Tan, Y.-W., Stormer, H. L., and Kim, P. *Nature* **438**, 201–4 (2005).

[5] Bolotin, K. I., Ghahari, F., Shulman, M. D., Stormer, H. L., and Kim, P. *Nature* **462**, 196–9 (2009).

[6] Katsnelson, M. I., Novoselov, K. S., and Geim, a. K. *Nat. Phys.* **2**, 620–625 (2006).

[7] Novoselov, K. S., Geim, A. K., Morozov, S. V., Jiang, D., Katsnelson, M. I., Grigorieva, I. V., Dubonos, S. V., and Firsov, A. A. *Nature* **438**, 197–200 (2005).

[8] Li, X., Cai, W., An, J., Kim, S., Nah, J., Yang, D., Piner, R., Velamakanni, A., Jung, I., Tutuc, E., Banerjee, S. K., Colombo, L., and Ruoff, R. S. *Science* **324**, 1312–4 (2009).

[9] Huang, P. Y., Ruiz-Vargas, C. S., van der Zande, A. M., Whitney, W. S., Levendorf, M. P., Kevek, J. W., Garg, S., Alden, J. S., Hustedt, C. J., Zhu, Y., Park, J., McEuen, P. L., and Muller, D. a. *Nature* **469**, 389–92 (2011).

[10] Sajjad, R. N., Sutar, S., Lee, J. U., and Ghosh, A. W. *Phys. Rev. B* **86**, 155412 (2012).

[11] Schlom, D. G., Guha, S., and Datta, S. *MRS Bull.* **33**, 1017–1025 (2008).

[12] Scott, J. F. *Science* **315**, 954–9 (2007).

[13] Setter, N., Damjanovic, D., Eng, L., Fox, G., Gevorgian, S., Hong, S., Kingon, A., Kohlstedt, H., Park, N. Y., Stephenson, G. B., Stolitchnov, I., Taganstev, A. K., Taylor, D. V., Yamada, T., and Streiffer, S. *J. Appl. Phys.* **100**, 051606 (2006).

[14] Dawber, M. and Scott, J. F. *Rev. Mod. Phys.* **77**, 1083–1130 (2005).

[15] Ahn, C. H., Rabe, K. M., and Triscone, J.-M. *Science* **303**, 488–91 (2004).

[16] Schlom, D. G., Chen, L.-Q., Eom, C.-B., Rabe, K. M., Streiffer, S. K., and Triscone, J.-M. *Annu. Rev. Mater. Res.* **37**, 589–626 (2007).

[17] Martin, L., Chu, Y.-H., and Ramesh, R. *Mater. Sci. Eng., R* **68**, 89–133 (2010).

[18] Lee, W., Han, H., Lotnyk, A., Schubert, M. A., Senz, S., Alexe, M., Hesse, D., Baik, S., and Gösele, U. *Nat. Nanotechnol.* **3**, 402–7 (2008).

[19] Hong, X., Posadas, a., Zou, K., Ahn, C., and Zhu, J. *Phys. Rev. Lett.* **102**, 2–5 (2009).

[20] Hong, X., Hoffman, J., Posadas, a., Zou, K., Ahn, C. H., and Zhu, J. *Appl. Phys. Lett.* **97**, 033114 (2010).

[21] Song, E. B., Lian, B., Min Kim, S., Lee, S., Chung, T.-K., Wang, M., Zeng, C., Xu, G., Wong, K., Zhou, Y., Rasool, H. I., Seo, D. H., Chung, H.-J., Heo, J., Seo, S., and Wang, K. L. *Appl. Phys. Lett.* **99**, 042109 (2011).

[22] Hsieh, C.-Y., Chen, Y.-T., Tan, W.-J., Chen, Y.-F., Shih, W. Y., and Shih, W.-H. *Appl. Phys. Lett.* **100**, 113507 (2012).

[23] Zheng, Y., Ni, G.-X., Toh, C.-T., Zeng, M.-G., Chen, S.-T., Yao, K., and Ozyilmaz, B. *Appl. Phys. Lett.* **94**, 163505 (2009).

[24] Ni, G.-X., Zheng, Y., Bae, S., Tan, C. Y., Kahya, O., Wu, J., Hong, B. H., Yao, K., and Özyilmaz, B. *ACS Nano* **6**, 3935–42 (2012).

[25] Zheng, Y., Ni, G.-X., Toh, C.-T., Tan, C.-Y., Yao, K., and Ozyilmaz, B. *Phys. Rev. Lett.* **105**, 5–8 (2010).

[26] Raghavan, S., Stolichnov, I., Setter, N., Heron, J.-S., Tosun, M., and Kis, A. *Appl. Phys. Lett.* **100**, 023507 (2012).

[27] Wallace, P. *Phys. Rev.* **71**, 622–634 (1947).

[28] Scott, B. W. and Leburton, J.-P. *IEEE Trans. Nanotechnol.* **10**, 1113–1119 (2011).

[29] Song, H. S., Li, S. L., Miyazaki, H., Sato, S., Hayashi, K., Yamada, A., Yokoyama, N., and Tsukagoshi, K. *Sci. Rep.* **2**, 337 (2012).

[30] Fratini, S. and Guinea, F. *Phys. Rev. B* **77**, 195415– (2008).

[31] Pirkle, A., Chan, J., Venugopal, A., Hinojos, D., Magnuson, C. W., McDonnell, S., Colombo, L., Vogel, E. M., Ruoff, R. S., and Wallace, R. M. *Appl. Phys. Lett.* **99**, 122108 (2011).

[32] Bolotin, K., Sikes, K., Jiang, Z., Klima, M., Fudenberg, G., Hone, J., Kim, P., and Stormer, H. *Solid State Commun.* **146**, 351–355 (2008).

[33] Haigh, S. J., Gholinia, A., Jalil, R., Romani, S., Britnell, L., Elias, D. C., Novoselov, K. S., Ponomarenko, L. A., Geim, A. K., and Gorbachev, R. *Nat. Mater.* **11**, 764–7 (2012).

[34] Xu, H., Chen, Y., Zhang, J., and Zhang, H. *Small* **8**, 2833–40 (2012).

[35] Na, P. S., Kim, H., So, H.-M., Kong, K.-J., Chang, H., Ryu, B. H., Choi, Y., Lee, J.-O., Kim, B.-K., Kim, J.-J., and Kim, J. *Appl. Phys. Lett.* **87**, 093101 (2005).

[36] Pascal-Levy, Y., Shifman, E., Pal-Chowdhury, M., Kalifa, I., Rabkin, T., Shtempluck, O., Razin, A., Kochetkov, V., and Yaish, Y. *Phys. Rev. B* **86**, 115445 (2012).

[37] Shim, M., Back, J., Ozel, T., and Kwon, K.-W. *Phys. Rev. B* **71**, 205411 (2005).

[38] Lee, J., Ryu, S., Yoo, K., Choi, I., Yun, W., and Kim, J. *J. Phys. Chem. C* **111**, 12504–12507 (2007).

[39] Radosavljević, M., Freitag, M., Thadani, K. V., and Johnson, A. T. *Nano Lett.* **2**, 761–764 (2002).

[40] Wang, H., Wu, Y., Cong, C., Shang, J., and Yu, T. *ACS Nano* **4**, 7221–8 (2010).

[41] Robert-Peillard, A. and Rotkin, S. *IEEE Trans. Nanotechnol.* **4**, 284–288 (2005).

[42] Gorbachev, R. V., Mayorov, A. S., Savchenko, A. K., Horsell, D. W., and Guinea, F. *Nano Lett.* **8**, 1995–9 (2008).

[43] Cheianov, V. V., Fal'ko, V., and Altshuler, B. L. *Science* **315**, 1252–5 (2007).

[44] Waser, R. *Nanoelectronics and Information Technology: Advanced Electronic Materials and Novel Devices.* John Wiley & Sons, (2003).

[45] Lines, M. E. and Glass, A. A. M. *Principles and Applications of Ferroelectrics and Related Materials.* Oxford University Press, (1977).

[46] Karthik, J. and Martin, L. W. *Phys. Rev. B* **84**, 024102 (2011).

[47] Merz, W. J. *J. Appl. Phys.* **27**, 938 (1956).

[48] Wurfel, P. and Batra, I. *Phys. Rev. B* **8**, 5126–5133 (1973).

[49] Bae, C., Zierold, R., Montero, J., Kim, H., Shin, H., Bachmann, J., and Nielsch, K. *J. Mater. Chem. C* (2013).

[50] Wicklein, S., Sambri, A., Amoruso, S., Wang, X., Bruzzese, R., Koehl, A., and Dittmann, R. *Appl. Phys. Lett.* **101**, 131601 (2012).

[51] Eason, R., editor. *Pulsed Laser Deposition of Thin Films.* John Wiley & Sons, Inc., Hoboken, NJ, USA, (2006).

[52] Bhaviripudi, S., Jia, X., Dresselhaus, M. S., and Kong, J. *Nano Lett.* **10**, 4128–33 (2010).

[53] Lin, Y.-C., Jin, C., Lee, J.-C., Jen, S.-F., Suenaga, K., and Chiu, P.-W. *ACS Nano* **5**, 2362–8 (2011).

[54] Pintilie, L., Vrejoiu, I., Hesse, D., and Alexe, M. *J. Appl. Phys.* **104**, 114101 (2008).

[55] Karthik, J., Damodaran, A. R., and Martin, L. W. *Adv. Mater.* **24**, 1610–5 (2012).

[56] Siddons, G. P., Merchin, D., Back, J. H., Jeong, J. K., and Shim, M. *Nano Lett.* **4**, 927–931 (2004).

[57] Ozel, T., Gaur, A., Rogers, J. A., and Shim, M. *Nano Lett.* **5**, 905–11 (2005).

[58] Giessibl, F. J. *Rev. Mod. Phys.* **75**, 949–983 (2003).

[59] Gruverman, A., Auciello, O., and Tokumoto, H. *Annu. Rev. Mater. Sci.* **28**, 101–123 (1998).

[60] McMorrow, D. *Elements of modern X-ray physics.* Wiley,, Hoboken :, 2nd ed. edition, (2011).

[61] Vincent, A. *Molecular Symmetry and Group Theory: A Programmed Introduction to Chemical Application.* John Wiley & Sons, (1977).

[62] Basko, D. M., Piscanec, S., and Ferrari, a. C. *Phys. Rev. B* **80**, 1–10 (2009).

[63] Cançado, L. G., Jorio, A., Ferreira, E. H. M., Stavale, F., Achete, C. A., Capaz, R. B., Moutinho, M. V. O., Lombardo, A., Kulmala, T. S., and Ferrari, A. C. *Nano Lett.* **11**, 3190–6 (2011).

[64] Malard, L., Pimenta, M., Dresselhaus, G., and Dresselhaus, M. *Phys. Rep.* **473**, 51–87 (2009).

[65] Kalbac, M., Reina-Cecco, A., Farhat, H., and Kong, J. *ACS Nano* **4**, 6055–6063 (2010).

[66] Kohn, W. *Phys. Rev. Lett.* **2**, 393–394 (1959).

[67] Bonini, N., Lazzeri, M., Marzari, N., and Mauri, F. *Phys. Rev. Lett.* **99**, 1–4 (2007).

[68] Tsang, J. C., Freitag, M., Perebeinos, V., Liu, J., and Avouris, P. *Nat. Nanotechnol.* **2**, 725–30 (2007).

[69] Choi, Y. S., Sung, J., Kang, S. J., Cho, S. H., Hwang, I., Hwang, S. K., Huh, J., Kim, H.-C., Bauer, S., and Park, C. *Adv. Funct. Mater.* , n/a–n/a (2012).

[70] Paruch, P., a. B. Posadas, Dawber, M., Ahn, C. H., and McEuen, P. L. *Appl. Phys. Lett.* **93**, 132901 (2008).

[71] Martin, J., Akerman, N., Ulbricht, G., Lohmann, T., Smet, J. H., von Klitzing, K., and Yacoby, a. *Nat. Phys.* **4**, 144–148 (2007).

[72] Zhang, Y., Brar, V. W., Girit, C., Zettl, A., and Crommie, M. F. *Nat. Phys.* **5**, 722–726 (2009).

[73] Chiu, H.-Y., Perebeinos, V., Lin, Y.-M., and Avouris, P. *Nano Lett.* **10**, 4634–9 (2010).

[74] Gysel, R., Stolichnov, I., Tagantsev, A. K., Riester, S. W. E., Setter, N., Salvatore, G. A., Bouvet, D., and Ionescu, A. M. *Appl. Phys. Lett.* **94**, 263507 (2009).

[75] Yamada, M., Nada, N., Saitoh, M., and Watanabe, K. *Appl. Phys. Lett.* **62**, 435 (1993).

[76] Mueller, T., Xia, F., Freitag, M., Tsang, J., and Avouris, P. *Phys. Rev. B* **79**, 1–6 (2009).

[77] Kong, Y., Xu, J., Li, B., Chen, S., Huang, Z., Zhang, L., Liu, S., Yan, W., Liu, H., Xie, X., Shi, L., Li, X., and Zhang, G. *Opt. Mater.* **27**, 471–473 (2004).

[78] Hammoum, R., Fontana, M., Bourson, P., and Shur, V. *Applied Physics A* **91**, 65–67 (2007).

[79] Das, A., Pisana, S., Chakraborty, B., Piscanec, S., Saha, S. K., Waghmare, U. V., Novoselov, K. S., Krishnamurthy, H. R., Geim, A. K., Ferrari, A. C., and Sood, A. K. *Nat. Nanotechnol.* **3**, 210–5 (2008).

[80] Lemme, M. C., Koppens, F. H. L., Falk, A. L., Rudner, M. S., Park, H., Levitov, L. S., and Marcus, C. M. *Nano Lett.* **11**, 4134–7 (2011).

[81] Liu, C.-H., Dissanayake, N. M., Lee, S., Lee, K., and Zhong, Z. *ACS Nano* **6**, 7172–6 (2012).

[82] Gorbachev, R. V., Mayorov, A. S., Savchenko, A. K., Horsell, D. W., and Guinea, F. *Nano Lett.* **8**, 1995–9 (2008).

[83] Nam, S.-G., Ki, D.-K., Park, J. W., Kim, Y., Kim, J. S., and Lee, H.-J. *Nanotechnology* **22**, 415203 (2011).

[84] Park, J., Ahn, Y. H., and Ruiz-Vargas, C. *Nano Lett.* **9**, 1742–6 (2009).

[85] Gabor, N. M., Song, J. C. W., Ma, Q., Nair, N. L., Taychatanapat, T., Watanabe, K., Taniguchi, T., Levitov, L. S., and Jarillo-Herrero, P. *Science* **334**, 648–52 (2011).

[86] Rao, G., Freitag, M., Chiu, H.-Y., Sundaram, R. S., and Avouris, P. *ACS Nano* **5**, 5848–54 (2011).

[87] Graham, M. W., Shi, S.-F., Ralph, D. C., Park, J., and McEuen, P. L. *Nat. Phys.* **9**, 103–108 (2012).

[88] Lee, E. J. H., Balasubramanian, K., Weitz, R. T., Burghard, M., and Kern, K. *Nat. Nanotechnol.* **3**, 486–90 (2008).

[89] Kwak, J., Chu, J. H., Choi, J.-K., Park, S.-D., Go, H., Kim, S. Y., Park, K., Kim, S.-D., Kim, Y.-W., Yoon, E., Kodambaka, S., and Kwon, S.-Y. *Nat. Commun.* **3**, 645 (2012).

[90] Peng, Z., Yan, Z., Sun, Z., and Tour, J. M. *ACS Nano* **5**, 8241–7 (2011).

[91] Zhou, M., Pasquale, F. L., Dowben, P. A., Boosalis, A., Schubert, M., Darakchieva, V., Yakimova, R., Kong, L., and Kelber, J. A. *J. Phys.: Condens. Matter* **24**, 072201 (2012).